Circadian clock disruption engages the DREAM complex in suppressing cellular health.

Isabela Santos Valentim[1], Francisco Javier Romero-Expósito[2], Katjana Schwab[1], Melike Bayar[1], Konstantin Riege[1], Martin Fischer[1], María Olmedo[2], Steve Hoffmann[1] and Maria A. Ermolaeva[1, 3, *].

1- Leibniz Institute on Aging – Fritz Lipmann Institute (FLI), Beutenbergstrasse 11, 07745 Jena, Germany.

2- Department of Genetics University of Sevilla, Av. Reina Mercedes s/n, 41012 Sevilla, Spain.

3- Cluster of Excellence Balance of the Microverse, Friedrich Schiller University Jena, Jena, Germany.

*- corresponding author: maria.ermolaeva@leibniz-fli.de

Abstract.

Circadian clock disruption and lack of sleep impair health of cells and organs, but mechanisms remain elusive. Here, we used multi-omics, molecular and functional assays in three model systems (*C. elegans*, human retinal cells and mouse brain) to identify the DREAM complex as a ubiquitous health repressor acting downstream of clock impairment. We show that clock

dysfunction aberrantly activates DREAM leading to simultaneous de-regulation of multiple cellular processes. The affected activities including translation, stress responses and OXPHOS are basic and ubiquitous, explaining pan-cellular decline induced by impaired clock and sleep. Accordingly, inhibition of DREAM restores healthy homeostasis and alleviates de-regulation of adaptive mechanisms in clock-impaired nematodes and human cells. This restorative effect occurs amid persisting clock dysfunction, suggesting that DREAM ablation uniquely uncouples circadian clock impairments from their negative effects on health. Our study coins DREAM as a new therapeutic target for preserving organismal fitness under re-current circadian dysfunction.

Introduction.

Circadian clock impairment and sleep deprivation have disruptive impact on multiple aspects of organismal fitness from cognition to the immune response[1-3]. This multifaceted influence can partially be explained by the requirement of sleep for the fluid flow and molecular damage clearance in the brain[4], with central nervous system (CNS) mediating a plethora of organismal responses[5]. A parallel hypothesis could be that sleep deprivation and circadian disruption affect master regulatory pathways, which control fundamental aspects of the cellular physiology and thereby modulate function of multiple cell types. The discovery of such core regulatory mechanisms could be an important step towards developing interventions that restore

homeostasis under circadian misalignment and sleep deprivation. Here, we used RNAi against the *C. elegans* PER orthologue *lin-42* to induce persistent but moderate clock disruption as a mimetic of lifestyle-inflicted clock irregularities. We next applied this intervention in *C. elegans* models of proteostasis stress and accelerated aging followed by proteomics, molecular and functional assays. In addition, transcriptomic analyses in mice with altered circadian behavior and in PER1 knock down human cells were conducted. These tests validated the causal contribution of clock disruption to homeostatic impairments especially in the context of additional cellular stress. We found a plethora of conserved and ubiquitously expressed molecular targets to be altered by the clock perturbation in line with the multifold loss of health under clock impairment. Finally, we revealed the worm DRM complex (DP, Rb and MuvB) and its related mammalian DREAM complex (DP, RB-like, E2F4 and MuvB) as a core regulator of clock-altered pathway activities and found that pharmacological and genetic inhibition of DREAM alleviates molecular and organismal dysfunction instigated by clock distortion.

Main.

<u>Moderate distortion of the circadian clock leads to tissue dysfunction in combination with physiological stress.</u>

In *C. elegans*, we employed RNAi-mediated gene inactivation to knock down a core component of the circadian clock PER/*lin-42*[6-10]. The complete loss of *lin-42* function was previously found to cause accelerated aging and early death in the nematodes[11]. This result is consistent with recent findings observing reduced longevity and increased prevalence of cellular stress in sleep deprived *D. melanogaster* and mice[12]. Unlike complete clock inactivation, our main interest was to test organismal effects of partial clock impairment, which is conceptually comparable to occasional loss of circadian function due to lack of sleep in mammals. We therefore opted for the RNAi-mediated gene knockdown (KD) approach instead of using loss of function mutants. We found that *lin-42* RNAi treatment from the L1 larval stage indeed caused the disruption of the clock-dependent molting process of *C. elegans* (Figure 1B and S1A) without causing a subsequent reduction of lifespan (Figure 1C) in line with the envisaged moderate clock impairment. Because previous studies in mice and *D. melanogaster* suggested that sleep deprivation induces cellular stress[12], we next asked if moderate circadian clock disruption would cause loss of tissue function in combination with additional stressors. In these experiments, we used transgenic protein aggregation models to inflict endogenous physiological stress in the body wall muscle of *C. elegans*. Specifically, we used nematodes expressing human amyloid-β peptide and polyglutamine coupled YFP protein in body wall muscle tissue (*unc-54p::human Aβ1-42* and *unc-54p::Q40::YFP* transgenic strains respectively)[13,14]. Interestingly, *lin-42* inactivation from the L1 larval stage significantly enhanced muscle dysfunction and whole-body paralysis in both

transgenic models (Figure 1D and S2A). A similar trend was observed also in transgenic animals treated with *lin-42* RNAi from the pre-adult L4 larval stage (Figures S2B and C). These results showed that clock disruption during adulthood is sufficient for causing decline of tissue homeostasis in concert with stress[3,15,16]. At the same time, developmental clock distortion had a stronger impact on the lifelong tissue functionality consistent with the highest prevalence and importance of sleep and coordinated quiescence during growth and development across species[17-22]. Finally, we found that RNAi inactivation of the downstream clock gene *lin-14*[23-25] caused enhanced paralysis of the *unc-54p::Q40::YFP* animals similar to the knock down of the upstream master regulator *lin-42* (Figure S2D). This result validates clock disruption as a mechanism linking *lin-42* inactivation to tissue dysfunction under stress. Collectively, we found that moderate but persistent clock impairment triggers organ dysfunction in combination with physiological stressors.

<u>Clock disruption elicits expression changes of chromatin components and regulators of DNA metabolism.</u>

To elucidate the molecular mechanisms linking clock disruption to organ frailty, we performed unbiased proteomics analysis of the animals exposed to *lin-42* RNAi from L1 and L4 stages (Figure 2A and S4A) detecting the total of 5.358 protein groups (Table S1-S2). The whole

proteome principal component analysis (PCA) showed a clear separation between *lin-42* RNAi treated and empty vector (EV) exposed control cohorts in the L1 treatment setting (Figure 2B). A subsequent gene set enrichment analysis of the proteins differentially expressed between animals treated with *lin-42* and control RNAi from the L1 stage revealed a significant enrichment of the gene ontology terms associated with chromatin organization and DNA metabolism (Figure 2C and Table S3). In parallel, the unbiased volcano plot analysis performed on the same set of proteins revealed different histone variants as the most clearly up-regulated protein sub-group (Figure 2D). Collectively, these two independent and unbiased whole proteome analyses indicated that chromatin changes are possibly associated with the cellular effects of the *lin-42* knock down (Figure 2F). To identify the putative core regulators linking *lin-42* inactivation to chromatin re-organization, we next computationally extracted the proteins, which contributed strongest to the separation between *lin-42* RNAi and EV control proteomes along the PC1 in Figure 2B (Table S4), and analyzed these by using the STRING protein-protein interaction assessment tool[26]. Interestingly, the strongest observed network included the key DRM complex component *lin-35*[27] and known DRM/DREAM targets and associated proteins such as histones *his-41*/H2BC and *htz-1*/H2A.Z2, and histone binding proteins *hcp-6*/NCAPD3 and *capg-2*/NCAPG2[28-30] (Figure S3, Table S5). Notably, DRM and its mammalian counterpart DREAM have been implicated in chromatin remodeling and gene expression regulation[31,32], in matching with the strong impact of clock disruption on chromatin components observed in Figures 2C and

2D. In addition to *lin-35* being a key contributor to proteome segregation along the PC1, most of individual DRM subunits and some of DRM-associated histones were upregulated in animals exposed to *lin-42* RNAi from both L1 and L4 stages (Figure 2E, Tables S6 and S7). Moreover, comparable DRM/DREAM-associated proteins contributed substantially to the PC1-separation in both L1- and L4-treated cohorts (Figure S3 and S4A-C, Tables S4 and S5). Overall, stronger molecular changes were seen following the L1-initiated clock disruption in line with the starker impact of the earlier treatment on the organismal health (Figure 1D, Figures S2A-C). These findings uncover the DREAM complex as a key molecular target of the circadian clock disruption, and demonstrate that the molecular effects of clock impairment are similar between development and adulthood, although they differ in magnitude.

<u>DRM/DREAM complex subunits and histones mediate tissue dysfunction in response to circadian clock disruption.</u>

To validate the involvement of the DRM/DREAM complex in the tissue dysfunction caused by circadian clock disruption, we performed co-knock downs of *lin-42* and individual DRM subunits by double RNAi exposure of the *unc-54p::Q40::YFP* animals. In these tests, we focused on RNAi treatment initiated at the L1 larval stage because of the stronger functional response observed in this setting previously (Figure 3A). Strikingly, we found that RNAi-

mediated depletion of DRM subunits *lin-9*, *lin-54* and *lin-53* reversed muscle paralysis caused by the *lin-42* gene knock down in the *unc-54p::Q40::YFP* animals, with *lin-53* inactivation showing the strongest reversal effect (Figure 3B-D). Notably, our double RNAi approach was effective in suppressing both genes simultaneously as seen with the example of *lin-42*/*lin-53* co-suppression (Figure S5A). At the same time, knock down of other canonical DRM subunits such as *lin-37*, *lin-52* and *lin-35* did not affect tissue dysfunction elicited by the *lin-42* RNAi (Figure S5B-D) demonstrating selective involvement of the distinct DRM/DREAM subunits in the effects of circadian clock. Moreover, we showed that RNAi-mediated depletion of the *htz-1*/H2A.Z2 histone variant found to be associated with the DRM/DREAM complex in our STRING analysis (Figure S3) and in literature[29], also rescued enhanced paralyses of the *unc-54p::Q40::YFP* nematodes treated with the *lin-42* RNAi (Figure 3E). Collectively, our results indicated that the enhanced activity of specific DRM/DREAM complex variants might mediate the negative impact of clock inactivation on tissue homeostasis under stress. Our data also suggested that increased abundance of specific DRM/DREAM-associated histones might play a role in this process by altering chromatin composition and broadly blunting gene expression with possible effect on the adaptive cellular activities. In line with the hypothesis of broad gene expression blunting, YFP expression was progressively reduced with age in *unc-54p::Q40::YFP* animals exposed to *lin-42* RNAi (Figure S6A and B), and this effect was reversed in worms co-treated with the anti-DRM *lin-53* RNAi. At the same time, relative YFP aggregation was progressively

increased with age in the *lin-42* RNAi exposed animals, and this distortion was also reversed by the co-knock down of the *lin-53* DRM subunit in line with respectively impaired and restored ability to counteract proteostasis stress (Figure 3F).

Clock disruption interferes with fundamental cellular activities in a DRM/DREAM-dependent manner.

We next used Western blot analysis to test if the increased abundance of histones in *lin-42* KD animals was indeed regulated by DRM/DREAM. Consistent with the proteomics data shown in Figure 2D, *lin-42* RNAi treatment resulted in elevated expression of most histone variants tested, and this elevation was reversed by the additional knock down of *lin-53* in all cases (Figure 4A-E, Figures S7 and S8). Notably, the differential expression between control, *lin-42* KD and *lin-42/lin-53* co-knockdown cohorts was reflected also at the mRNA level at least for some of the histone variants (Figure 4F). These results suggested that *lin-53*/DRM might act as a transcriptional inducer of the histone genes (Figure 4G) in line with previous reports of the dual repressor-activator role of DREAM and DRM in gene expression[28,33].

Subsequently, we asked what molecular pathways become de-regulated in *lin-42* knockdown nematodes and re-instated in *lin-42/lin-53* double knockdown animals, representing molecular targets affected by the circadian clock disruption in a DRM/DREAM-dependent manner. *lin-53*

inactivation was chosen due to its strongest ability of reversing the negative health effects of the *lin-42* KD (Figure 3D), and because *lin-53*/RBBP4 was reported to mediate the interaction between DRM/DREAM and histones[34,35]. The comparative proteomics analysis of *lin-42* KD, *lin-42/lin-53* co-knockdown and EV RNAi control-exposed cohorts (Figure 5A and Table S8) strikingly revealed simultaneous alterations of multiple mechanisms implicated in both basal homeostasis of the cell and in adaptive stress responses. For instance, detoxification mechanisms such as xenobiotic metabolism (Figure 5B and Table S9) and pathways implicated in the antioxidant response (Figures 5C, D and S9A, B and Table S9) were found to be suppressed by *lin-42* KD and restored by the co-knockdown of *lin-53*. The antioxidant response was represented by simultaneous de-regulation of four distinct metabolic entities implicated in counteracting oxidative stress: aldehyde dehydrogenase protein family (Figure 5C)[36], glutathione metabolism (Figure 5D)[37], tryptophan catabolism by kynurenine pathway (Figure S9A) with intermediates known to exert ROS scavenging roles[38-40], and short chain dehydrogenase protein family implicated in xenobiotic and antioxidant defense responses (Figure S9B)[41,42]. The outstanding enrichment of antioxidant mechanisms among the DRM-dependent clock targets fits well with oxidative stress being the primary cause of the early demise in sleep deprived *Drosophila* and mice[12]. At the same time, xenobiotic detoxification responses were previously found to be de-regulated in the livers of Per1/Per2 double-knockout mice suffering from clock impairment[43], in line with our present findings. In addition, metabolic plasticity pathways such as

glycolysis and fatty acid β-oxidation[44] were diminished by *lin-42* KD and reinstated by *lin-53* co-inactivation (Figure 5E and F, Table S9), while key bioenergetics activities of mitochondria – TCA cycle and OXPHOS, were dampened by *lin-42* inactivation and partially rescued by *lin-53* RNAi co-treatment (Figure S9C and D, Table S9). Finally, the expression of ECM components collagens was downregulated in *lin-42* RNAi-exposed animals and restored by *lin-42*/*lin-53* co-knockdown (Figure 5G, Table S9). Notably, both decline of metabolic plasticity and reduced expression of collagens are associated with loss of organ function during aging[44-46], establishing a link between clock disruption and accelerated tissue impairment. Moreover, an impairment of metabolic adaptive capacity was previously observed in Per1/Per2 deficient mouse livers[43]. The cell-protective interplay between metabolic and detoxification activities regulated by DRM/DREAM and clock can also be envisaged because tryptophan catabolism by kynurenine pathway is one of the key cellular sources of nicotinamide adenine dinucleotide (NAD+)[47]– an energy carrier and enzymatic co-factor with key roles in mitochondrial maintenance and bioenergetics fitness, and with capacity to delay metabolic aging[47]. The strong enrichment of metabolic pathways among DRM-dependent clock targets is in line with the large body of human clinical data designating clock and sleep dysfunction as confounding factors of metabolic diseases such as diabetes, obesity and cardio-vascular disorders[48,49].

Interestingly, also basal cellular activities such as Pol II transcription and splicing were differentially affected in our experimental system showing upregulation following clock

distortion and re-blunting by co-knock down of *lin-53* (Figure 5H and S9E; Table S9). Of note, increased speed of Pol II transcription and elevated splicing were recently revealed to be hallmarks and functional drivers of physiological aging[50], and the interference of the *lin-42* KD with both processes provided yet another putative *lin-53*/DRM-dependent link between clock disruption and premature organismal demise. Finally, we observed mitochondrial ribosome, cytosolic ribosome, ribosome biogenesis and translational proteins to be strongly downregulated by *lin-42/lin-53* co-knock down (Figure 5I, 5J, S9F and S9G; Table S9) suggesting that DRM/DREAM modulates these essential activities in the context of clock disruption. Because inhibition of translation is known to improve proteostasis by reducing protein folding stress[51-53], the strong blunting of this process at multiple levels likely contributes to superior capacity of *lin-42*/*lin-53* double KD to reduce polyQ aggregates compared to *lin-42* only inactivated worms (Figure 3F).

Notably, by comparing the list of clock and DREAM co-targets depicted in Figures 5 and S9 to the previously published DREAM ChiP-Seq *C. elegans* dataset[29], we determined that only few of these genes are located in the close proximity to the relevant genomic DREAM binding sites (Table S10). This finding speaks in favor of indirect chromatin- and histone-dependent regulation of these targets by DRM/DREAM, which is also supported by all of the functional and molecular data we obtained thus far. Overall, we found that clock disruption causes multiple alterations of basal and adaptive cellular functions that are reduced by co-knockdown of

DRM/DREAM likely by affecting histone levels and chromatin structure (Figure 5H). The amplitude of changes in the individual adaptive pathways was not drastic, but in combination, these alterations have the potential to impede cellular homeostasis and flexibility at multiple levels contributing to health decline associated with clock and sleep impairments.

The DREAM-clock interaction is evolutionary conserved, and pharmacological inhibition of DREAM restores homeostasis under clock disruption.

To test if clock impairment interferes with the adaptive mechanisms also in mammalian tissues, we turned to publicly available transcriptomic data of mice affected by circadian disruption. Interestingly, a recent study explored circadian impairments and their alleviation by time-restricted feeding in brains of transgenic mice expressing the Alzheimer's disease (AD)-associated variant of the human amyloid precursor protein[54], which is conceptually similar to our experiments combining clock impairment with proteostasis stress in *C. elegans*. We therefore re-analyzed the transcriptomic data provided in this study (Table S11) focusing on the beginning (ZT0) and the end (ZT12) of the murine sleep period (Figure S10A). The initial over-representation analysis of the genes de-regulated by the circadian impairment (transgenic ad libitum fed cohort, TG ALF) and re-instated by the clock-resetting treatment (transgenic cohort with time-restricted feeding, TG TRF) revealed ribosome, oxidative phosphorylation,

mitochondria-linked terms such as thermogenesis and Parkison's disease, and extracellular matrix (ECM) as most enriched categories in both ZT0 and ZT12 samples (Figure S10B and Tables S12-S17). We next quantitatively confirmed that the expression of the mitochondrial (Figure 6A, Table S18), OXPHOS (Figure 6B and Table S18), ribosome (Figure S11B and Table S19), and ECM (Figure S11C and Table S19) genes was indeed de-regulated and restored in a clock-driven manner, similar to the clock-orchestrated DRM/DREAM-dependent dynamics of these pathways observed in *C. elegans* (Figures 5 and S9). Interestingly, the de-regulation triggered by clock impairment was stronger at ZT0 compared to ZT12 for most of the above gene sets, making a plausible link with the restorative role of the deep (slow wave) sleep that is least prevalent at the end of the sleep period[55,56]. Collectively, our tests revealed that similar fundamental and potentially restorative cellular processes are affected by circadian impairments in nematodes and mice.

We next turned to a human cell culture system to test if PER inactivation is indeed sufficient to disrupt circadian clock and if inhibition of the DREAM complex can alleviate clock-related molecular impairments in the background of PER deficiency. Here we used siRNA-mediated knockdown of PER1 in human retinal pigment epithelial (RPE) cells, and we used the DYRK1A inhibitor Harmine to pharmacologically suppress DREAM function, as seen in previous reports[57,58]. PER1 was chosen as the key cycling PER paralogue across mammalian tissues as shown in a recent report[59]. We found that PER1 knockdown was robust (Figure 6C) and indeed

sufficient to cause clock impairments as seen by altered expression of CLOCK and CRY2 core clock genes in qPCR and transcriptomic tests (Figures 6D and S12A). Importantly, Harmine did not restore the clock in PER1-depleted cells (Figures 6D and S12A), but caused expected induction of p53 target genes[60], which was not accompanied by a down-regulation of cell cycle genes[32,61], as seen by qPCR and high throughput transcriptomic analysis (Figures S12B and S12C, and Table 21), validating Harmine's function as a DREAM inhibitor. Collectively, these results confirmed our hypothesis that the restorative effect of DREAM inhibition on the homeostasis of clock-disrupted cells is independent of clock reinstatement and likely occurs downstream of an impaired clock.

Subsequently, we turned to deeper high-throughput transcriptomic analysis of PER1- and Harmine-treated RPE cells to identify the key homeostatic mechanisms regulated by clock in a DREAM-dependent manner in human cells (Table S20). Strikingly, our findings were similar to observations obtained in the nematode and mouse models. For instance, we found that mitochondrial and OXPHOS genes are downregulated by clock disruption and reinstated by co-inhibition of DREAM also in human cells (Figure 6E and 6F; Table S22), revealing mitochondria and OXPHOS as the most consistently clock-regulated entities across species and cell types. Interestingly, this observation is consistent with the recently discovered key involvement of mitochondria and OXPHOS in the induction of sleep and damage clearance during sleep[62,63]. Moreover, ribosome and ribosome biogenesis genes, and genes encoding the

components of the transcriptional machinery showed opposite expression dynamics between clock-disrupted and DREAM co-inhibited cells (Figure S12D-F; Table S23). These results matched the observations in nematodes and mice, and clearly suggested that similar fundamental cellular activities are altered by clock impairment in a DREAM-dependent fashion across species.

Since the DREAM inhibitor Harmine is bioavailable *in vivo*[64,65], we tested if Harmine treatment could alleviate the decline of fitness elicited by *lin-42* KD in *C. elegans* comparably to the genetic inactivation of DRM. We found that co-administration of Harmine in *unc-54p::Q40::YFP* animals exposed to *lin-42* RNAi indeed reversed the paralysis induced by clock disruption in this model (Figures 6F, and S11G). These results demonstrate that pharmacological inhibition of DREAM is an intriguing *in vivo* tool for rescuing the health of organisms affected by persistent circadian dysfunction. In summary, our study revealed that clock disruption interferes with multiple fundamental and adaptive cellular pathways and coined the DREAM complex as a key mediator of these negative effects. Based on our findings, we propose DREAM to be a promising novel intervention target for the repair of cellular functions under lack of coordinated organismal quiescence such as sleep (Figure 6G).

Discussion.

In this study, we combined omics, genetics, functional and molecular analyses in three model systems to elucidate the molecular basis of the body-wide health decline that is caused by a persistent deregulation of the circadian clock and sleep[3,15,16]. As a result, we discovered for the first time that clock disruption engages the DREAM complex and associated chromatin changes in distorting a multitude of fundamental and adaptive cellular activities ranging from translation and splicing to OXPHOS, oxidative stress response and ECM remodeling. In the context of existing knowledge about DREAM complex, circadian cycle and the protective role of histones and chromatin [66,67], our new analysis suggests that under normal physiological conditions the DREAM-inflicted chromatin compaction likely protects the genomic DNA from molecular damage associated with wakefulness [68,69]. Conversely, during the quiescence phase of the circadian cycle, the chromatin compaction is reversed [70] facilitating expression of the genes implicated in the detoxification and repair (Figure S13). Indeed, many repair activities including autophagy and DNA repair are known to be most effective during sleep [71,72], in line with our hypothesis and model. In this context, sleep and clock impairments interfere with chromatin re-opening in a DREAM-dependent manner thereby blocking repair activities and sensitizing cells to stress and damage to trigger a decline of organ functions. This phenomenon is particularly evident in the organisms predisposed to stress such as nematodes expressing aggregation prone human A beta or Q40-linked YFP proteins. Because the affected molecular mechanisms are so fundamental, their alteration is likely to affect most cells in an organism, consistent with

published observations that circadian/sleep disruptions impair homeostasis of multiple organs[12,43,54]. Our hypothesis is also consistent with the large body of reports linking sleep deprivation to human diseases and inferior organismal responses to extrinsic stressors ranging from infections and cognitive challenges to exercise and diet[73-76]. In addition, our findings are in line with a recent report coining intestinal oxidative stress as the main cause of premature demise of *Drosophila* and mice chronically deprived of sleep[12]. We therefore lay out for the first time a mechanistic model that integrates and explains most of the current knowledge about organismal and cellular effects of disrupted sleep and circadian dysfunction. From the translational standpoint, we additionally show that pharmacological and genetic inhibition of the DREAM complex restores homeostasis of cells and organisms affected by circadian impairments. We demonstrate that this restoration process does not require clock reinstatement making it unique among existing approaches to alleviating sleep and circadian dysfunction that rely on the eventual repair of clock and/or sleep[77-79]. The potential DREAM-targeting intervention is thus uniquely suited for cases when clock reinstalment is limited by the genetic, environmental (e.g. polar night/day) or professional entities (e.g. shift work).

Notably, while omics data comparison between the species revealed pathways that are consistently regulated by clock in all systems, the direction of regulation occasionally differed between nematodes and mammals (mice and human cells). For example, ribosome abundance was dampened by the inactivation of DREAM in clock-disrupted *C. elegans*, while opposite

(down- and up-regulation respectively) was seen in clock impaired and reinstated human cells and mouse brains. This interesting difference may be on the one hand indicative of the differential tissue maintenance strategies of post-mitotic *C. elegans* and mammalian organs/cultures that rely on cell proliferation for functional repair. Alternatively, cell- and tissue-specific effects may play a role: while our *C. elegans* findings reflect the most abundant responses at the whole organism level, the mouse and human discoveries are restricted to one tissue (brain) or even one cell type (human RPE cells). For example, the expression of extracellular matrix components is reduced by clock impairment in *C. elegans* (Figure 6G) while it becomes elevated in the mouse brain (Figure S11C). Such a difference is putatively meaningful from the physiological standpoint: while at the whole organism level higher ECM abundance is supportive of tissue integrity, in the brain elevated ECM levels may impede sleep-associated damage clearance, which requires effective perfusion of the brain tissue by the cerebrospinal fluid[4,80]. The combination of all organs may also explain the greater number of clock-modulated pathways observed in our *C. elegans* analysis compared to mouse and human tests. Accordingly, several of the clock-affected *C. elegans* responses (such as shifts in metabolic plasticity mechanisms, oxidative stress response and xenobiotic detoxification response) overlap with previously reported changes in mouse tissues such as liver[43] and intestine[12] that are not covered by our present analyses.

Finally, our findings suggest that the DREAM complex simultaneously regulates multiple cellular functions via controlling the abundance of histones and (likely) the accessibility of the respective chromatin regions. This model is supported by the previous report detecting high abundance of the histone variant HTZ-1/H2A.Z in the gene body of DRM/DREAM-repressed cell cycle targets[29], with HTZ-1/H2A.Z being one of the principle histones we found to cooperate with DRM/DREAM in de-regulating the cellular resilience of clock-distorted animals. Consistently, only a minor fraction of the molecular targets altered by clock disruption in a DREAM-dependent manner harbors relevant DREAM binding sites in their promoter regions (Table S9), supporting an indirect regulation by modulation of the chromatin structure. Interestingly, this histone-dependent mode of DREAM action is distinct from the well-documented capacity of DRM/DREAM to repress multiple pathways implicated in DNA repair[33,81-83], which relies on the direct binding of DREAM to the regulatory elements of affected genes. Notably, also the predominantly implicated DRM/DREAM subunits differ between DNA repair and circadian functions of DRM/DREAM with *lin-52*, *dpl-1*, *efl-1* and *lin-35* having the strongest impact in DNA repair[81] and *lin-9*, *lin-54* and *lin-53* regulating the consequences of the circadian disruption. Our findings thus support the likely existence of two different modes of how specific variants of the DREAM complex regulate complex gene expression networks: (a) via direct binding and recruitment of co-factors and/or co-repressors[31,32] and (b) via changes in histone composition and chromatin structure ([29] and this study). The dependency of the circadian

response on the presence of particular DREAM subunits opens a possibility of targeted interventions that modulate the "sleep-specific" role of DREAM without interfering with its activities in other cellular processes. An additional path of mitigating potential side effects derives from our new mechanistic model presented in Figure S13: we propose that the administration of DREAM inhibitors can be restricted to the biologically intended quiescence period of a given organism (e.g. nighttime for humans), thus replicating the natural circadian fluctuations of DREAM activity. In follow-up studies, we anticipate to functionally test these hypotheses *in vivo* in vertebrates.

Acknowledgements: We thank the Proteomics Core Facility at FLI, and especially Joanna Kirkpatrick, Erika Kelmer Sacramento, Emilio Cirri, and Therese Dau for supporting this study. The Core Facility Next Generation Sequencing (Ivonne Goerlich, Marco Groth) of the FLI is gratefully acknowledged for their technological support in library preparation and mRNA sequencing. Marcus Wildt for his support in data structure and coding. The FLI is a member of the Leibniz Association and is financially supported by the Federal Government of Germany and the State of Thuringia. ISV was supported by the doctoral fellowship from the Leibniz Graduate School on Aging (LGSA). ME was supported by the EU-ESF Thüringer Aufbaubank funding (2019 FGR 0082). ME is currently funded by the Carl-Zeiss-Stiftung via IMPULS consortium and is a member of Cluster of Excellence Balance of the Microverse funded by the Deutsche Forschungsgemeinschaft (DFG). ME is also funded by the ERC CoG LifeLongFit of the European Commission. *C. elegans* strains were obtained from the Caenorhabditis Genetics

Center (CGC), which is funded by NIH. FJRE is supported by a contract of the VPPI-University of Sevilla (Contratos de Personal Investigador en Formación). Work in the Olmedo lab is supported by the grant PID2022-139009OB-I00, funded by MCIN/AEI/10.13039/501100011033/FEDER, UE.

Author contributions: ME and ISV conceptualized and designed the study; ISV, FJRE, KS and MB performed experiments; ME, MO, MF and SH supervised data analysis and visualization; ME, ISV, FJRE, KS, MB, MF, KR, SH and MO analyzed the data; ISV prepared figures and tables, and performed statistical analyses; ME wrote the manuscript, ISV, MF, SH and MO reviewed the manuscript.

Data availability: The mass spectrometry proteomics data have been deposited to the ProteomeXchange Consortium via the PRIDE (Perez-Riverol et al., 2019) and MassIVE repositories with the respective dataset identifiers PXD024273 and MSV000091972. The RNA-seq data have been deposited to the NCBI Gene Expression Omnibus (GEO) with data set identifier GSE250018.

Conflict of interest: ME and ISV are listed as inventors on a patent application, which is based on some of the described findings.

Bibliography:

1 Banks, S. & Dinges, D. F. Behavioral and physiological consequences of sleep restriction. *J Clin Sleep Med* **3**, 519-528 (2007).

2 Zielinski, M. R. *et al.* Chronic sleep restriction elevates brain interleukin-1 beta and tumor necrosis factor-alpha and attenuates brain-derived neurotrophic factor expression. *Neurosci Lett* **580**, 27-31 (2014). https://doi.org:10.1016/j.neulet.2014.07.043

3 Knutson, K. L., Spiegel, K., Penev, P. & Van Cauter, E. The metabolic consequences of sleep deprivation. *Sleep Med Rev* **11**, 163-178 (2007). https://doi.org:10.1016/j.smrv.2007.01.002

4 Xie, L. *et al.* Sleep drives metabolite clearance from the adult brain. *Science* **342**, 373-377 (2013). https://doi.org:10.1126/science.1241224

5 Plog, B. A. & Nedergaard, M. The Glymphatic System in Central Nervous System Health and Disease: Past, Present, and Future. *Annu Rev Pathol* **13**, 379-394 (2018). https://doi.org:10.1146/annurev-pathol-051217-111018

6 Jeon, M., Gardner, H. F., Miller, E. A., Deshler, J. & Rougvie, A. E. Similarity of the C. elegans developmental timing protein LIN-42 to circadian rhythm proteins. *Science* **286**, 1141-1146 (1999). https://doi.org:10.1126/science.286.5442.1141

7 Tennessen, J. M., Gardner, H. F., Volk, M. L. & Rougvie, A. E. Novel heterochronic functions of the Caenorhabditis elegans period-related protein LIN-42. *Dev Biol* **289**, 30-43 (2006). https://doi.org:10.1016/j.ydbio.2005.09.044

8 Nelson, M. D. & Raizen, D. M. A sleep state during C. elegans development. *Curr Opin Neurobiol* **23**, 824-830 (2013). https://doi.org:10.1016/j.conb.2013.02.015

9 Monsalve, G. C., Van Buskirk, C. & Frand, A. R. LIN-42/PERIOD controls cyclical and developmental progression of C. elegans molts. *Curr Biol* **21**, 2033-2045 (2011). https://doi.org:10.1016/j.cub.2011.10.054

10 Lamberti, M. L. *et al.* Regulation of the circadian clock in C. elegans by clock gene homologs kin-20 and lin-42. *bioRxiv*, 2023.2004.2013.536481 (2023). https://doi.org:10.1101/2023.04.13.536481

11 Kalfalah, F. *et al.* Crosstalk of clock gene expression and autophagy in aging. *Aging (Albany NY)* **8**, 1876-1895 (2016). https://doi.org:10.18632/aging.101018

12 Vaccaro, A. *et al.* Sleep Loss Can Cause Death through Accumulation of Reactive Oxygen Species in the Gut. *Cell* **181**, 1307-1328 e1315 (2020). https://doi.org:10.1016/j.cell.2020.04.049

13 Morley, J. F., Brignull, H. R., Weyers, J. J. & Morimoto, R. I. The threshold for polyglutamine-expansion protein aggregation and cellular toxicity is dynamic and influenced by aging in Caenorhabditis elegans. *Proc Natl Acad Sci U S A* **99**, 10417-10422 (2002). https://doi.org:10.1073/pnas.152161099

14 McColl, G. *et al.* Utility of an improved model of amyloid-beta (Abeta(1)(-)(4)(2)) toxicity in Caenorhabditis elegans for drug screening for Alzheimer's disease. *Mol Neurodegener* **7**, 57 (2012). https://doi.org:10.1186/1750-1326-7-57

15 in *Sleep Disorders and Sleep Deprivation: An Unmet Public Health Problem The National Academies Collection: Reports funded by National Institutes of Health* (eds H. R. Colten & B. M. Altevogt) (2006).

16 Fishbein, A. B., Knutson, K. L. & Zee, P. C. Circadian disruption and human health. *J Clin Invest* **131** (2021). https://doi.org:10.1172/JCI148286

17 Kayser, M. S. & Biron, D. Sleep and Development in Genetically Tractable Model Organisms. *Genetics* **203**, 21-33 (2016). https://doi.org:10.1534/genetics.116.189589

18 Seugnet, L., Suzuki, Y., Donlea, J. M., Gottschalk, L. & Shaw, P. J. Sleep deprivation during early-adult development results in long-lasting learning deficits in adult Drosophila. *Sleep* **34**, 137-146 (2011). https://doi.org:10.1093/sleep/34.2.137

19 Alrousan, G., Hassan, A., Pillai, A. A., Atrooz, F. & Salim, S. Early Life Sleep Deprivation and Brain Development: Insights From Human and Animal Studies. *Front Neurosci* **16**, 833786 (2022). https://doi.org:10.3389/fnins.2022.833786

20 Anafi, R. C., Kayser, M. S. & Raizen, D. M. Exploring phylogeny to find the function of sleep. *Nat Rev Neurosci* **20**, 109-116 (2019). https://doi.org:10.1038/s41583-018-0098-9

21 Siegel, J. M. Do all animals sleep? *Trends Neurosci* **31**, 208-213 (2008). https://doi.org:10.1016/j.tins.2008.02.001

22 Trojanowski, N. F. & Raizen, D. M. Call it Worm Sleep. *Trends Neurosci* **39**, 54-62 (2016). https://doi.org:10.1016/j.tins.2015.12.005

23 Ambros, V. & Horvitz, H. R. The lin-14 locus of Caenorhabditis elegans controls the time of expression of specific postembryonic developmental events. *Genes Dev* **1**, 398-414 (1987). https://doi.org:10.1101/gad.1.4.398

24 Hristova, M., Birse, D., Hong, Y. & Ambros, V. The Caenorhabditis elegans heterochronic regulator LIN-14 is a novel transcription factor that controls the developmental timing of transcription from the insulin/insulin-like growth factor gene ins-33 by direct DNA binding. *Mol Cell Biol* **25**, 11059-11072 (2005). https://doi.org:10.1128/MCB.25.24.11059-11072.2005

25 Van Wynsberghe, P. M. & Pasquinelli, A. E. Period homolog LIN-42 regulates miRNA transcription to impact developmental timing. *Worm* **3**, e974453 (2014). https://doi.org:10.4161/21624054.2014.974453

26 Szklarczyk, D. *et al.* The STRING database in 2023: protein-protein association networks and functional enrichment analyses for any sequenced genome of interest. *Nucleic Acids Res* **51**, D638-D646 (2023). https://doi.org:10.1093/nar/gkac1000

27 Harrison, M. M., Ceol, C. J., Lu, X. & Horvitz, H. R. Some C. elegans class B synthetic multivulva proteins encode a conserved LIN-35 Rb-containing complex distinct from a NuRD-like complex. *Proc Natl Acad Sci U S A* **103**, 16782-16787 (2006). https://doi.org:10.1073/pnas.0608461103

28 Esterlechner, J. *et al.* LIN9, a subunit of the DREAM complex, regulates mitotic gene expression and proliferation of embryonic stem cells. *PLoS One* **8**, e62882 (2013). https://doi.org:10.1371/journal.pone.0062882

29 Latorre, I. *et al.* The DREAM complex promotes gene body H2A.Z for target repression. *Genes Dev* **29**, 495-500 (2015). https://doi.org:10.1101/gad.255810.114

30 Uxa, S. *et al.* DREAM and RB cooperate to induce gene repression and cell-cycle arrest in response to p53 activation. *Nucleic Acids Res* **47**, 9087-9103 (2019). https://doi.org:10.1093/nar/gkz635

31 Sadasivam, S. & DeCaprio, J. A. The DREAM complex: master coordinator of cell cycle-dependent gene expression. *Nat Rev Cancer* **13**, 585-595 (2013). https://doi.org:10.1038/nrc3556

32 Fischer, M. & Muller, G. A. Cell cycle transcription control: DREAM/MuvB and RB-E2F complexes. *Crit Rev Biochem Mol Biol* **52**, 638-662 (2017). https://doi.org:10.1080/10409238.2017.1360836

33 Tabuchi, T. M. *et al.* Chromosome-biased binding and gene regulation by the Caenorhabditis elegans DRM complex. *PLoS Genet* **7**, e1002074 (2011). https://doi.org:10.1371/journal.pgen.1002074

34 Asthana, A. *et al.* The MuvB complex binds and stabilizes nucleosomes downstream of the transcription start site of cell-cycle dependent genes. *Nat Commun* **13**, 526 (2022). https://doi.org:10.1038/s41467-022-28094-1

35 Koliopoulos, M. G. *et al.* Structure of a nucleosome-bound MuvB transcription factor complex reveals DNA remodelling. *Nat Commun* **13**, 5075 (2022). https://doi.org:10.1038/s41467-022-32798-9

36 Singh, S. *et al.* Aldehyde dehydrogenases in cellular responses to oxidative/electrophilic stress. *Free Radic Biol Med* **56**, 89-101 (2013). https://doi.org:10.1016/j.freeradbiomed.2012.11.010

37 Tan, M. *et al.* Glutathione system enhancement for cardiac protection: pharmacological options against oxidative stress and ferroptosis. *Cell Death Dis* **14**, 131 (2023). https://doi.org:10.1038/s41419-023-05645-y

38 Genestet, C. *et al.* Scavenging of reactive oxygen species by tryptophan metabolites helps Pseudomonas aeruginosa escape neutrophil killing. *Free Radic Biol Med* **73**, 400-410 (2014). https://doi.org:10.1016/j.freeradbiomed.2014.06.003

39 Ramirez Ortega, D. *et al.* On the Antioxidant Properties of L-Kynurenine: An Efficient ROS Scavenger and Enhancer of Rat Brain Antioxidant Defense. *Antioxidants (Basel)* **11** (2021). https://doi.org:10.3390/antiox11010031

40 Christen, S., Peterhans, E. & Stocker, R. Antioxidant activities of some tryptophan metabolites: possible implication for inflammatory diseases. *Proc Natl Acad Sci U S A* **87**, 2506-2510 (1990). https://doi.org:10.1073/pnas.87.7.2506

41 Zolkipli, Z., Pedersen, C. B., Lamhonwah, A. M., Gregersen, N. & Tein, I. Vulnerability to oxidative stress in vitro in pathophysiology of mitochondrial short-chain acyl-CoA dehydrogenase deficiency: response to antioxidants. *PLoS One* **6**, e17534 (2011). https://doi.org:10.1371/journal.pone.0017534

42 Kavanagh, K. L., Jornvall, H., Persson, B. & Oppermann, U. Medium- and short-chain dehydrogenase/reductase gene and protein families : the SDR superfamily: functional and structural diversity within a family of metabolic and regulatory enzymes. *Cell Mol Life Sci* **65**, 3895-3906 (2008). https://doi.org:10.1007/s00018-008-8588-y

43 Yiran Bu, S. C., Mengcheng Ruan, Libang Wu, Hualin Wang, Na Li, Xiuju Zhao, Xiaoli Yu, Zhiguo Liu. Per1/Per2 double knockout transcriptome analysis reveals circadian regulation of hepatic lipid metabolism. *Food Science and Human Wellness* **12**, 1716-1729 (2023). https://doi.org:https://doi.org/10.1016/j.fshw.2023.02.034.

44 Espada, L. *et al.* Loss of metabolic plasticity underlies metformin toxicity in aged Caenorhabditis elegans. *Nat Metab* **2**, 1316-1331 (2020). https://doi.org:10.1038/s42255-020-00307-1

45 Ewald, C. Y., Landis, J. N., Porter Abate, J., Murphy, C. T. & Blackwell, T. K. Dauer-independent insulin/IGF-1-signalling implicates collagen remodelling in longevity. *Nature* **519**, 97-101 (2015). https://doi.org:10.1038/nature14021

46 Statzer, C., Park, J. Y. C. & Ewald, C. Y. Extracellular Matrix Dynamics as an Emerging yet Understudied Hallmark of Aging and Longevity. *Aging Dis* **14**, 670-693 (2023). https://doi.org:10.14336/AD.2022.1116

47 Castro-Portuguez, R. & Sutphin, G. L. Kynurenine pathway, NAD(+) synthesis, and mitochondrial function: Targeting tryptophan metabolism to promote longevity and healthspan. *Exp Gerontol* **132**, 110841 (2020). https://doi.org:10.1016/j.exger.2020.110841

48 Spiegel, K., Knutson, K., Leproult, R., Tasali, E. & Van Cauter, E. Sleep loss: a novel risk factor for insulin resistance and Type 2 diabetes. *J Appl Physiol (1985)* **99**, 2008-2019 (2005). https://doi.org:10.1152/japplphysiol.00660.2005

49 Gangwisch, J. E. *et al.* Short sleep duration as a risk factor for hypertension: analyses of the first National Health and Nutrition Examination Survey. *Hypertension* **47**, 833-839 (2006). https://doi.org:10.1161/01.HYP.0000217362.34748.e0

50 Debes, C. *et al.* Ageing-associated changes in transcriptional elongation influence longevity. *Nature* **616**, 814-821 (2023). https://doi.org:10.1038/s41586-023-05922-y

51 Syntichaki, P., Troulinaki, K. & Tavernarakis, N. eIF4E function in somatic cells modulates ageing in Caenorhabditis elegans. *Nature* **445**, 922-926 (2007). https://doi.org:10.1038/nature05603

52 Hansen, M. *et al.* Lifespan extension by conditions that inhibit translation in Caenorhabditis elegans. *Aging Cell* **6**, 95-110 (2007). https://doi.org:10.1111/j.1474-9726.2006.00267.x

53 Clay, K. J., Yang, Y., Clark, C. & Petrascheck, M. Proteostasis is differentially modulated by inhibition of translation initiation or elongation. *Elife* **12** (2023). https://doi.org:10.7554/eLife.76465

54 Whittaker, D. S. *et al.* Circadian modulation by time-restricted feeding rescues brain pathology and improves memory in mouse models of Alzheimer's disease. *Cell Metab* **35**, 1704-1721 e1706 (2023). https://doi.org:10.1016/j.cmet.2023.07.014

55 Dijk, D. J. Regulation and functional correlates of slow wave sleep. *J Clin Sleep Med* **5**, S6-15 (2009).

56 Bes, F., Schulz, H., Navelet, Y. & Salzarulo, P. The distribution of slow-wave sleep across the night: a comparison for infants, children, and adults. *Sleep* **14**, 5-12 (1991). https://doi.org:10.1093/sleep/14.1.5

57 Litovchick, L., Florens, L. A., Swanson, S. K., Washburn, M. P. & DeCaprio, J. A. DYRK1A protein kinase promotes quiescence and senescence through DREAM complex assembly. *Genes Dev* **25**, 801-813 (2011). https://doi.org:10.1101/gad.2034211

58 MacDonald, J. *et al.* A Systematic Analysis of Negative Growth Control Implicates the DREAM Complex in Cancer Cell Dormancy. *Mol Cancer Res* **15**, 371-381 (2017). https://doi.org:10.1158/1541-7786.MCR-16-0323-T

59 Mure, L. S. *et al.* Diurnal transcriptome atlas of a primate across major neural and peripheral tissues. *Science* **359** (2018). https://doi.org:10.1126/science.aao0318

60 Dai, F. *et al.* A natural small molecule harmine inhibits angiogenesis and suppresses tumour growth through activation of p53 in endothelial cells. *PLoS One* **7**, e52162 (2012). https://doi.org:10.1371/journal.pone.0052162

61 Fischer, M., Grossmann, P., Padi, M. & DeCaprio, J. A. Integration of TP53, DREAM, MMB-FOXM1 and RB-E2F target gene analyses identifies cell cycle gene regulatory networks. *Nucleic Acids Res* **44**, 6070-6086 (2016). https://doi.org:10.1093/nar/gkw523

62 Haynes, P. R. *et al.* A neuron-glia lipid metabolic cycle couples daily sleep to mitochondrial homeostasis. *Nat Neurosci* (2024). https://doi.org:10.1038/s41593-023-01568-1

63 Sarnataro, R., Velasco, C. D., Monaco, N., Kempf, A. & Miesenböck, G. Mitochondrial origins of the pressure to sleep. *bioRxiv*, 2024.2002.2023.581770 (2024). https://doi.org:10.1101/2024.02.23.581770

64 Guan, Y., Louis, E. D. & Zheng, W. Toxicokinetics of tremorogenic natural products, harmane and harmine, in male Sprague-Dawley rats. *J Toxicol Environ Health A* **64**, 645-660 (2001). https://doi.org:10.1080/152873901753246241

65 Patel, K., Gadewar, M., Tripathi, R., Prasad, S. K. & Patel, D. K. A review on medicinal importance, pharmacological activity and bioanalytical aspects of beta-carboline alkaloid ''Harmine''. *Asian Pac J Trop Biomed* **2**, 660-664 (2012). https://doi.org:10.1016/S2221-1691(12)60116-6

66 Ljungman, M. & Hanawalt, P. C. Efficient protection against oxidative DNA damage in chromatin. *Mol Carcinog* **5**, 264-269 (1992). https://doi.org:10.1002/mc.2940050406
67 Phillips, E. O. N. & Gunjan, A. Histone variants: The unsung guardians of the genome. *DNA Repair (Amst)* **112**, 103301 (2022). https://doi.org:10.1016/j.dnarep.2022.103301
68 Zada, D. *et al.* Parp1 promotes sleep, which enhances DNA repair in neurons. *Mol Cell* **81**, 4979-4993 e4977 (2021). https://doi.org:10.1016/j.molcel.2021.10.026
69 Lewis, S. DNA damage drives sleep. *Nat Rev Neurosci* **23**, 69 (2022). https://doi.org:10.1038/s41583-021-00550-9
70 Zada, D., Bronshtein, I., Lerer-Goldshtein, T., Garini, Y. & Appelbaum, L. Sleep increases chromosome dynamics to enable reduction of accumulating DNA damage in single neurons. *Nat Commun* **10**, 895 (2019). https://doi.org:10.1038/s41467-019-08806-w
71 Bellesi, M., Bushey, D., Chini, M., Tononi, G. & Cirelli, C. Contribution of sleep to the repair of neuronal DNA double-strand breaks: evidence from flies and mice. *Sci Rep* **6**, 36804 (2016). https://doi.org:10.1038/srep36804
72 Pastore, N. *et al.* Nutrient-sensitive transcription factors TFEB and TFE3 couple autophagy and metabolism to the peripheral clock. *EMBO J* **38** (2019). https://doi.org:10.15252/embj.2018101347
73 Garbarino, S., Lanteri, P., Bragazzi, N. L., Magnavita, N. & Scoditti, E. Role of sleep deprivation in immune-related disease risk and outcomes. *Commun Biol* **4**, 1304 (2021). https://doi.org:10.1038/s42003-021-02825-4
74 Csipo, T. *et al.* Sleep deprivation impairs cognitive performance, alters task-associated cerebral blood flow and decreases cortical neurovascular coupling-related hemodynamic responses. *Sci Rep* **11**, 20994 (2021). https://doi.org:10.1038/s41598-021-00188-8
75 VanHelder, T. & Radomski, M. W. Sleep deprivation and the effect on exercise performance. *Sports Med* **7**, 235-247 (1989). https://doi.org:10.2165/00007256-198907040-00002
76 Theorell-Haglow, J. *et al.* Sleep duration is associated with healthy diet scores and meal patterns: results from the population-based EpiHealth study. *J Clin Sleep Med* **16**, 9-18 (2020). https://doi.org:10.5664/jcsm.8112
77 Vasey, C., McBride, J. & Penta, K. Circadian Rhythm Dysregulation and Restoration: The Role of Melatonin. *Nutrients* **13** (2021). https://doi.org:10.3390/nu13103480
78 Kramer, A. *et al.* Foundations of circadian medicine. *PLoS Biol* **20**, e3001567 (2022). https://doi.org:10.1371/journal.pbio.3001567
79 Izumida, T., Nakamura, Y., Sato, Y. & Ishikawa, S. The Association Between Sleeping Pill Use and Metabolic Syndrome in an Apparently Healthy Population in Japan: JMS-II Cohort Study. *J Epidemiol* **32**, 145-150 (2022). https://doi.org:10.2188/jea.JE20200361
80 Fultz, N. E. *et al.* Coupled electrophysiological, hemodynamic, and cerebrospinal fluid oscillations in human sleep. *Science* **366**, 628-631 (2019). https://doi.org:10.1126/science.aax5440
81 Bujarrabal-Dueso, A. *et al.* The DREAM complex functions as conserved master regulator of somatic DNA-repair capacities. *Nat Struct Mol Biol* **30**, 475-488 (2023). https://doi.org:10.1038/s41594-023-00942-8
82 Jaber, S., Toufektchan, E., Lejour, V., Bardot, B. & Toledo, F. p53 downregulates the Fanconi anaemia DNA repair pathway. *Nat Commun* **7**, 11091 (2016). https://doi.org:10.1038/ncomms11091
83 Walston, H., Iness, A. N. & Litovchick, L. DREAM On: Cell Cycle Control in Development and Disease. *Annu Rev Genet* **55**, 309-329 (2021). https://doi.org:10.1146/annurev-genet-071819-103836

1

Figure legends.

Fig. 1 | **Knockdown of *lin-42*/PER impairs clock-controlled developmental timing and exacerbates aggregation-driven tissue failure. (a)** Luminometry experimental design: Animals expressing a luciferase reporter of food intake were used. Feeding during larval stages triggers an increase of luminescence while quiescence and lack of feeding during molting stages leads to a decrease of signal. **(b)** Developmental timing (duration of the larval stages L1-L4) of control (ctrl), *lin-42* RNAi knock-down, *lin-42(n1089)* mutant and *lin-42(ok2385)* mutant animals is shown. Control (EV RNAi) and *lin-42* RNAi cohorts were established in the wild type (N2 Bristol strain) background. *lin-42(n1089)* mutant and *lin-42(ok2385)* mutant animals were fed with EV RNAi, and all worms were fed with D-Luciferin. Larval stage durations were quantified at 20ºC based on relevant luminescence signals. Each dot represents one animal; average and S.E.M values are plotted. n=5-20 worms per condition in each trial, and results of 4 independent trials are combined. One-way ANOVA was used for the statistical assessment, two-tailed *p* values were computed, *-$p<0.05$; **-$p<0.01$; ***-$p<0.001$; ****-$p<0.0001$. **(c)** Wild-type (N2) worms were age-synchronized and fed with EV (ctrl) or *lin-42* RNAi from the L1 stage. Survival was scored daily. Animals were transferred to new plates every second day until adulthood day 10 (AD10), and every fourth day thereafter. n=140 worms per condition, graph is representative of three independent experiments. Significance was measured by the Log-rank Mantel-Cox test, two-tailed *p* values were computed. ns, not significant. **(d)** Age-synchronized populations of *unc-54*p::Q40::YFP animals were fed with EV (ctrl) or *lin-42* RNAi from the L1 stage. Paralysis was scored daily. Worms were transferred to new plates every second day. n=140 worms per condition, graph is representative of three independent experiments. Significance was measured by the Log-rank Mantel-Cox test, two-tailed *p* values were computed. ****-$p<0.000001$.

Fig. 2 | **Clock disruption triggers changes in histone expression, chromatin organization, and DRM/DREAM complex abundance. (a)** Experimental design. **(b)** Principal component analysis comparing whole proteomes of wild-type *C. elegans* treated with EV or *lin-42* RNAi from the L1 stage is shown. Proteins were extracted on AD2, and small dots are representative of independent replica samples, n=800 worms per replica. **(c)** Bar plot of significantly enriched (FDR ≤ 0.05) GO terms among proteins upregulated (Average Log_2 expression FC>0) between *lin-42* and EV RNAi-treated animals is shown. **(d)** Volcano plot depicting differently expressed

proteins between *lin-42* and EV RNAi-treated cohorts is shown, with histones highlighted in red. The horizontal dashed line indicates a Q-value cutoff of 0.05 and the vertical lines - a $\log_2$ expression fold change cut-off of ≤0.58. **(e)** Heatmap of selected DRM/DREAM subunits and interactors is shown. The color code refers to $\log_2$ expression fold change values between *lin-42* and EV RNAi-treated cohorts; RNAi treatments from both L1 and L4 stages are included. **(f)** Mechanistic model is presented. The complete data and calculations for panels **b-e** can be found in Tables S1, S3 and S6-7 respectively.

Fig. 3 | **Inactivation of the DRM/DREAM complex reverses functional impairments induced by clock disruption. (a)** Left caption reminds of elevated DRM/DREAM abundance in clock-impaired animals; right caption depicts the experimental design. **(b-e)** Age-synchronized *unc-54*p::Q40::YFP animals were fed with EV or *lin-42* RNAi in combination with RNAis targeting specific subunits/interactors of the DRM/DREAM complex from the L1 stage, paralysis was scored daily. Co-targeting with *lin-9* **(b)**, *lin-54* **(c)**, *lin-53* **(d),** and DRM/DREAM interactor *htz-1* **(e)** is shown. n=140 worms per condition, graphs are representative of at least three independent experiments. Significance was measured by the Log-rank Mantel-Cox test, two-tailed *p* values were computed. ****-$p<0.0001$. **(f)** *unc-54*p::Q40::YFP worms were age-synchronized, fed with indicated RNAi constructs from the L1 stage, and imaged at three different time points: L4, adulthood day 1 (AD1), and AD2. The number of aggregates divided by respective YFP intensity is shown, n=26-32 worms per condition, graph is representative of three independent experiments. Error bars are S.E.M. Significance was measured by one-way ANOVA within each age group separately and applying Sidak's multiple comparison test, two-tailed *p* values were computed. **-$p<0.01$; ****-$p<0.0001$; ns, not significant.

Fig. 4 | **Clock impairment elevates histone abundance in a DRM/DREAM-dependent manner. (a-d)** Wild type worms were age-synchronized and treated with indicated RNAi combinations from the L1 stage and until AD2. Expression of histones H1, H2, H3, and H4 was measured by immunoblot using tubulin as a loading control, and quantification is presented. Each graph combines the results of 5 independent treatments/immunoblots; n=800 worms in each condition. Error bars are S.E.M., representative immunoblot images are shown in panel **(e)** and full gels can be seen in Figure S7. **(f)** Worms were treated as in (a-d) and

mRNA expression levels of *his-24* (H1), *hil-2* (H1), and *his-29* (H2) were assessed by RT-qPCR. n=250 worms per condition, graphs are representative of three independent experiments. Error bars are S.E.M.; mRNA fold change was calculated by the ΔΔ Ct method. Significance was measured by one-way ANOVA within each group separately and applying Sidak's multiple comparisons test, two-tailed *p* values were computed. *-$p<0.05$; **-$p<0.01$; ***-$p<0.001$; ****-$p<0.0001$; ns, not significant. **(g)** Mechanistic summary of the findings is presented.

Fig. 5 | **Clock disruption interferes with fundamental cellular processes in a DRM/DREAM-dependent fashion. (a)** Experimental design. Worms were treated with indicated RNAi combinations and control (EV) RNAi from the L1 stage until AD2. Protein expression was resolved by proteomics. **(b-j)** Box plots showing relative expression (*ev+lin-42* over *ev*, and *lin-42+lin-53* over *ev* comparisons) of proteins belonging to xenobiotic metabolism **(b)**, aldehyde dehydrogenase pathway **(c)**, glutathione metabolism **(d)**, glycolysis **(e)**, fatty acid ß-oxidation **(f)**, collagens **(g),** transcription initiation **(h),** mitochondrial ribosome **(i),** and cytosolic ribosome **(j)** are presented. Individual proteins are shown as dots, the median fold change of each group is shown as a horizontal line; the upper and lower limits of the box plot indicate the first and third quartile and the whiskers extend 1.5 times the interquartile range from the limits of each box. n=800 worms per condition and 4 independent populations were measured in each case. Within each box plot, the significance was assessed by Mann-Whitney Wilcoxon rank-sum test, and Wilcoxon test was used for the comparison between the two sets of fold changes. Two-tailed *p* values were computed in all cases. *-$p<0.05$; **-$p<0.01$; ***-$p<0.001$; ****-$p<0.0001$. The lists and data of all included proteins can be found in Tables S8 (complete data) and S9 (box plot data). **(k)** Mechanistic model is depicted.

Fig. 6 **| The DREAM-clock relationship is evolutionary conserved and malleable by pharmacological DREAM inhibitors. (a-b)** Analysis of transcriptomic data from hippocampi of mice either wild type (WT) or expressing human AD-like APP variant (transgenic, TG, mice) either fed ad libitum (ALF) or subjected to time-restricted feeding (TLF, Whittaker et al., 2023). Data for ZT0 and ZT12 were analyzed. Box plots show $\log_2$ expression fold changes of mitochondrial **(a)** and OXPHOS (oxidative phosphorylation) **(b)** genes between indicated

conditions. Individual genes are shown as dots, the median fold change of each group is shown as a horizontal line; the upper and lower limits of the box plot indicate the first and third quartile, and the whiskers extend 1.5 times the interquartile range from the limits of each box. n=6-7 mice per condition. The lists and data of all genes can be found in Tables S11 (complete normalized counts data, as in the original publication), S12 (Log2FC calculations) and S18 (box plot data). **(c-d)** Human retinal pigment epithelial cells (RPE) cells were treated with control siRNA (siC1, 10 nM) or siRNA against PER1 (siPER1, 10 nM) for 48h and co-treated with Harmine (Har, 10μM) or DMSO (vehicle control) for 20h. Expression analysis of PER1 (**c**) and CLOCK (**d**) genes was performed by RT-qPCR (left panel) and mRNA sequencing (right panel) in the same cell extracts. Data is shown as mRNA expression fold changes calculated by the ΔΔCt method and transcript per million values (TPM) respectively. Data in the left panel is representative of 5 independent trials, and 4-5 independent samples were combined in the right panel. Significance was measured by one-way ANOVA within each group separately, and applying Sidak's multiple comparisons test, two-tailed *p* values were computed. *-$p<0.05$; **-$p<0.01$; ***-$p<0.001$; ****-$p<0.0001$; ns, not significant **(e-f)** High throughput transcriptomic analysis (mRNA sequencing) of the cells described in (c-d) was conducted. Box plots show $\log_2$ expression fold changes of mitochondrial **(e)** and OXPHOS **(f)** genes between indicated conditions. Individual genes are shown as dots, the median fold change of each group is shown as a horizontal line; the upper and lower limits of the boxplot indicate the first and third quartile and the whiskers extend 1.5 times the interquartile range from the limits of each box. n=4-5 independent cultures per condition. In **a**, **b**, **e** and **f**, the significance was assessed by Mann-Whitney Wilcoxon rank-sum test within each box plot, and Wilcoxon test was used for the comparison between the two respective sets of fold changes. Two-tailed *p* values were computed in all cases. *-$p<0.05$; **-$p<0.01$; ***-$p<0.001$; ****-$p<0.0001$; ns, not significant. The lists and data of all genes can be found in Tables S20 (complete data) and S22 (box plot data). **(g)** Age-synchronized population of *unc-54*p::Q40::YFP nematodes was treated with EV or *lin-42* RNAi from the L1 stage in plates containing either 0.1% DMSO (vehicle) or Harmine (Har, 60 μM). Paralysis was scored daily. n=140 worms per condition, graphs representative of three independent experiments. Significance was measured by the Log-rank Mantel-Cox test, two-tailed *p* values were computed. ****-$p<0.0001$. **(h)** The model depicting the role of DREAM in mediating cellular impairments downstream of disrupted clock is presented.

Fig. S1 | **RNAi-mediated inactivation of *lin-42*/PER interferes with clock-dependent developmental timing**. **(a)** Developmental timing (duration of molting stages M1-M4) of control (ctrl), *lin-42* RNAi knock-down, *lin-42(n1089)* mutant and *lin-42(ok2385)* mutant animals is shown. Control (EV RNAi) and *lin-42* RNAi cohorts were established in the wild type (N2 Bristol strain) background, *lin-42(n1089)* mutant and *lin-42(ok2385)* mutant animals were fed with EV RNAi, and all worms were fed with D-Luciferin. Molting stage durations were quantified at 20ºC based on relevant luminescence signals. Each dot represents one animal; average and S.E.M values are plotted. n=5-20 worms per condition in each trial, and results of 4 independent trials are combined. One-way ANOVA was used for the statistical assessment, two-tailed *p* values were computed *-$p<0.05$; **-$p<0.01$; ***-$p<0.001$; ****-$p<0.0001$.

Fig. S2 | **Clock disruption exacerbates muscle paralysis in *C. elegans* models of Alzheimer's and Huntington's diseases. (a)** *unc-54*p::human Aβ_{1-42} worms (GMC101 strain) were age-synchronized and treated with EV (ctrl) or *lin-42* RNAi from the L1 stage. Until the L4 stage the worms were cultivated at 20ºC and then shifted to 25ºC, to trigger amyloid-beta toxicity. **(b)** Age-synchronized population of *unc-54*p::Q40::YFP animals was fed with EV (ctrl) or *lin-42* RNAi from the L4 stage. **(c)** *unc-54*p::human Aβ_{1-42} worms were age-synchronized and treated with EV (ctrl) or *lin-42* RNAi from the L4 stage. The shift to 25ºC was performed as described in (a). **(d)** Age-synchronized population of *unc-54*p::Q40::YFP animals were fed with EV (ctrl) or *lin-14* RNAi from the L1 stage. Paralysis was scored daily in all cases (**a-d**). n=140 worms per condition, graphs show representative results of at least three independent experiments. Significance was measured by the Log-rank Mantel-Cox test, two-tailed *p* values were computed. *-$p<0.05$; ****-$p<0.0001$, ns, not significant.

Fig. S3 | **Protein-protein interaction analysis reveals DRM/DREAM complex as a putative central target of clock impairment.** STRING analysis was performed using version 11 (latest version at the time of the analysis) with the protein groups that contributed strongest to the PC1 separation in Fig. 2b (the complete list and data can be found in Table S4). The absolute rotational weight of the included proteins had a cutoff of >0.023, and 120 proteins had a significant network enrichment of $p<1.0e^{-16}$ (Table S5). Colored network nodes represent query proteins. Edges represent meaningful protein-protein associations. Turquoise and purple edges

represent known interactions, with purple depicting experimentally tested interactions. Green, red and blue edges represent predicted interactions, with green representing gene neighborhood, red – gene fusions, and blue – gene co-occurrence. Light green edges represent results of text mining, black edges – co-expression, and light blue edges – protein homology.

Fig. S4 | **Whole proteome changes are comparable between animals subjected to *lin-42*/PER inactivation during development and adulthood. (a)** Experimental design. **(b)** Whole-proteome principal component analysis of wild-type *C. elegans* treated with EV (ctrl) or *lin-42* RNAi from the L4 stage is shown. Small dots are representative of individual replicas, n=800 worms per sample. **(c)** STRING analysis using version 11 (latest version at the time of the analysis) was performed with the protein groups that contributed the strongest to the PC1 separation in Fig. S4b. The related source data can be found in Tables S2 (complete data) and S4 (STRING data). The absolute rotational weight of the proteins had a cutoff of >0.01, and 46 proteins had a significant network enrichment of $p<9.18e^{-12}$ (Table S5). Color code of nodes and edges is as explained in Figure S3.

Fig. S5 | **The interplay between DRM/DREAM and clock impairment demonstrates subunit specificity. (a)** 250 worms per condition were age-synchronized and treated with indicated RNAi combinations from the L1 stage, and *lin-42* and *lin-53* gene expression was measured by RT-qPCR on AD2. Graphs are representative of three independent experiments. Mean and S.E.M. values are presented. mRNA expression fold change was calculated by the ΔΔCt method. Significance was measured by unpaired t-test, two-tailed *p* values were computed. **-$p<0.01$; ***-$p<0.001$; ns, not significant. **(b-d)** *unc-54*p::Q40::YFP animals were age synchronized and fed from the L1 stage with EV or *lin-42* RNAi and in combination with RNAi against specific DREAM subunits or interactors: *lin-37* **(b)**, *lin-52* **(c)**, *lin-35* **(d)**. Paralysis was scored daily. n=140 worms per condition, graphs are representative of at least three independent experiments. Significance was measured by the Log-rank Mantel-Cox test, two-tailed *p* values were computed. ****-$p<0.0001$; *-$p<0.05$, ns, not significant.

Fig. S6 | ***lin-53*/DREAM inactivation restores protein homeostasis in clock-disrupted animals expressing polyglutamine-linked YFP.** *unc-54*p::Q40::YFP worms were age-synchronized and fed with indicated RNAi combinations from the L1 stage and imaged at three different time points: L4, AD1, and AD2; EV – empty vector control. **(a)** YFP intensity per total body area is shown. n=26-32 worms per condition, the graph is representative of three individual experiments. Error bars are S.E.M. Significance was measured by one-way ANOVA within each age group separately and using Sidak's multiple comparison test, two-tailed *p* values were computed. *-$p<0.05$; ****-$p<0.0001$; ns, not significant. **(b)** Representative images of AD2 *unc-54p*::Q40::YFP animals treated with indicated RNAi combinations. Worms were imaged in an AxioZoom v.16 microscope with 90x magnification and exposure time of 150 ms for YFP and 4.8 ms for brightfield imaging. The scale bar is 200 µm.

Fig. S7 | **Clock disruption enhances the expression of histones in a DRM/DREAM-dependent manner.** Representative full gel scans for Fig.4a-d. **(a)** H1, **(b)** H2B1L, **(c)** H3, **(d)** H4. Size-consistent bands used for quantification are marked by arrowheads. H= histone and T= tubulin.

Fig. S8 | **Clock disruption elevates the expression of histones in a DRM/DREAM-dependent manner. (a-b)** Worms were treated and analyzed as described in Figure 4a-d, using antibody specific to histone H2AZ. Representative full gel scans (left) and respective quantification (right) are shown. The graph summarizes results of five independent experiments. n=800 per condition and error bars are S.E.M. Significance was measured by one-way ANOVA, two-tailed *p* values were computed. ****-$p<0.0001$, ns, not significant.

Fig. S9 | **Circadian clock disruption interferes with fundamental cellular processes in a DRM/DREAM-dependent manner. (a-g)** Animals were treated and analyzed as described in Figure 5. Box plots show the relative expression of proteins involved in tryptophan metabolism **(a)**, short-chain dehydrogenases **(b)**, TCA cycle **(c)**, OXPHOS **(d)**, spliceosome **(e),** ribosome biogenesis **(f)**, and translation factors **(g)**. Individual proteins are shown as dots, the median fold change of each group is shown as a horizontal line; the upper and lower limits of the boxplot indicate the first and third quartile and the whiskers extend 1.5 times the interquartile

range from the limits of each box. n=800 per condition and 4 independent populations were measured. Within each box plot, the significance was assessed by Mann-Whitney Wilcoxon rank-sum test, and Wilcoxon test was used for the comparison between the two sets of fold changes. Two-tailed *p* values were computed in all cases. *-$p<0.05$; **-$p<0.01$; ***-$p<0.001$; ****-$p<0.0001$. The lists and data of all proteins can be found in Tables S8 (complete data) and S9 (box plot data).

Fig. S10 | **Same fundamental cellular activities are altered by clock disruption in mice and nematodes. (a)** Schematic summarizes the experimental design, and highlights the samples selected for the re-analysis. WT – wild type animals, TG – mice expressing human AD-like APP variant, ALF – *ad libitum* feeding, TRF – time restricted feeding. **(b)** Venn diagrams illustrate the overlap between opposite regulated genes in TG ALF versus WT ALF and TG TRF versus TG ALF comparisons at ZT0 and ZT12. Gene numbers and % of total gene set are depicted. Overlapping gene sets representing genes altered by clock disruption and restored by TRF treatment were used for the GO enrichment analysis. Bar plots of significantly enriched (FDR ≤ 0.05) GO terms are presented. Red color depicts similarities between effects of clock impairment in mice and nematodes. The data analysis is shown in Tables S13-17.

Fig. S11 **| Same fundamental cellular processes are altered by clock disruption in mice and nematodes. (a)** Experimental design is depicted, as described in Fig. S10a. **(b-c)** The transcriptomic data was analyzed as in Fig. 6a-b. Box plots showing relative expression of ribosome **(b)**, and extracellular matrix **(c)** genes are presented. Individual genes are shown as dots, the median fold change of each group is shown as a horizontal line; the upper and lower limits of the boxplot indicate the first and third quartile and the whiskers extend 1.5 times the interquartile range from the limits of each box. n=6-7 mice per condition. Within each box plot, the significance was assessed by Mann-Whitney Wilcoxon rank-sum test, and Wilcoxon test was used for the comparison between the two sets of fold changes. Two-tailed *p* values were computed in all cases. *-$p<0.05$; **-$p<0.01$; ***-$p<0.001$; ****-$p<0.0001$. The lists and data of all genes can be found in Tables S11 (complete data) and S19 (box plot data).

Fig. S12 | **Same fundamental cellular activities are regulated by clock/DREAM axis in nematodes and human cells. (a-f)** Human RPE cells were treated and analyzed as described in Fig. 6c-f, n=4-5 independent cultures per condition. Expression analysis of CRY2 **(a)** and p21 **(b)** gene is shown. RT-qPCR (left panel) and transcriptomic measurements (right panel) are presented as described in Fig. 6c-d. Significance was measured by one-way ANOVA within each group separately and applying Sidak's multiple comparisons test, two-tailed *p* values were computed. ****-$p<0.0001$. **(c)** Heatmap depicting expression of p53 target genes is presented with complete data shown in Table S20 and sorted data shown in Table S21. Color code refers to Z score values. **(d-f)** Transcriptomic data was analyzed as in Fig. 6e-f. Box plots showing relative expression of the ribosome **(d)**, ribosome biogenesis **(e)**, and RNA polymerase (transcription) **(f)** genes are presented. Individual genes are shown as dots, the median fold change of each group is shown as a horizontal line; the upper and lower limits of the boxplot indicate the first and third quartile and the whiskers extend 1.5 times the interquartile range from the limits of each box. Within each box plot, the significance was assessed by Mann-Whitney Wilcoxon rank-sum test, and Wilcoxon test was used for the comparison between the two sets of fold changes. Two-tailed *p* values were computed in all cases. *-$p<0.05$; **-$p<0.01$; ***-$p<0.001$; ****-$p<0.0001$. The list and data of all genes can be found in Tables S20 (complete data) and S23 (box plot data). **(g)** *unc-54*p::Q40::YFP nematodes was treated with EV or *lin-42* RNAi in plates containing either 0.1% DMSO (vehicle) or Harmine (Har, 40 μM). Paralysis was scored daily. n=140 worms per condition, graph is representative of three independent experiments. Significance was measured by the Log-rank Mantel-Cox test, two-tailed *p* values were computed. ****-$p<0.0001$.

Fig. S13 | **Mechanistic model describing the physiological role of DREAM in the circadian control of healthy homeostasis.** In the context of the current literature, our findings suggest that DREAM-induced chromatin compaction has a role in protecting genomic DNA from molecular damage induced by organismal activities linked to wakefulness. Conversely, during the quiescence/sleep phase of the circadian cycle, the chromatin compaction is reversed facilitating expression of the genes implicated in the detoxification and repair. The disruption of sleep and/or circadian cycle interferes with chromatin re-opening in a DREAM-dependent manner thereby blocking repair activities and sensitizing cells and organs to stress and damage. We propose to restrict the administration of DREAM inhibitors to the intended quiescence

phase of a given organism (e.g. nighttime for humans) in order to replicate the natural circadian fluctuations of DREAM activity, thus reducing potential side effects of the DREAM inhibition.

Figure 1

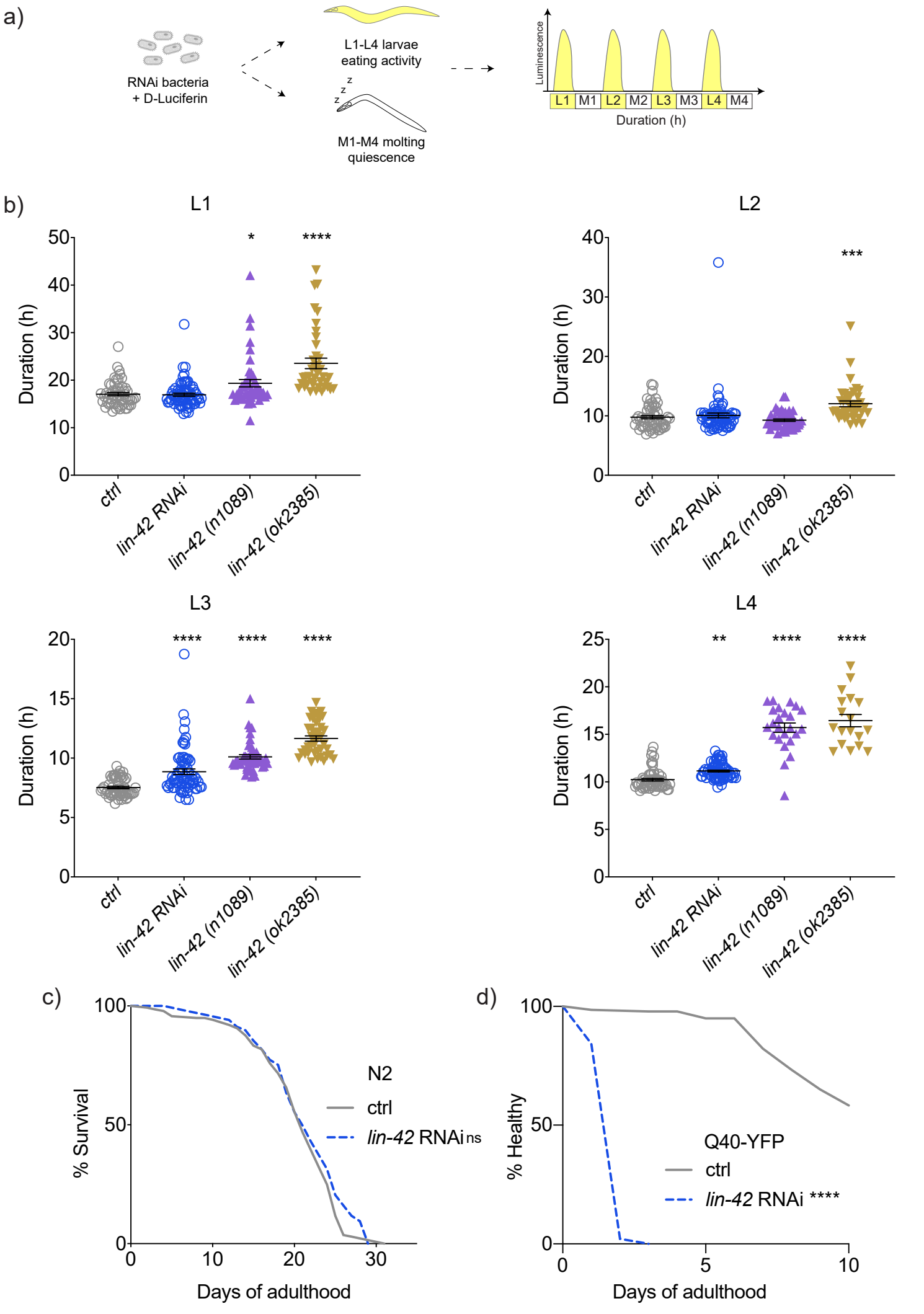
a)
RNAi bacteria
+ D-Luciferin
L1-L4 larvae
eating activity
M1-M4 molting
quiescence
Luminescence
L1 M1 L2 M2 L3 M3 L4 M4
Duration (h)
b)
L1
L2
L3
L4
Duration (h)
ctrl
lin-42 RNAi
lin-42 (n1089)
lin-42 (ok2385)
c)
% Survival
Days of adulthood
N2
ctrl
lin-42 RNAi ns
d)
% Healthy
Days of adulthood
Q40-YFP
ctrl
lin-42 RNAi ****

Figure 2

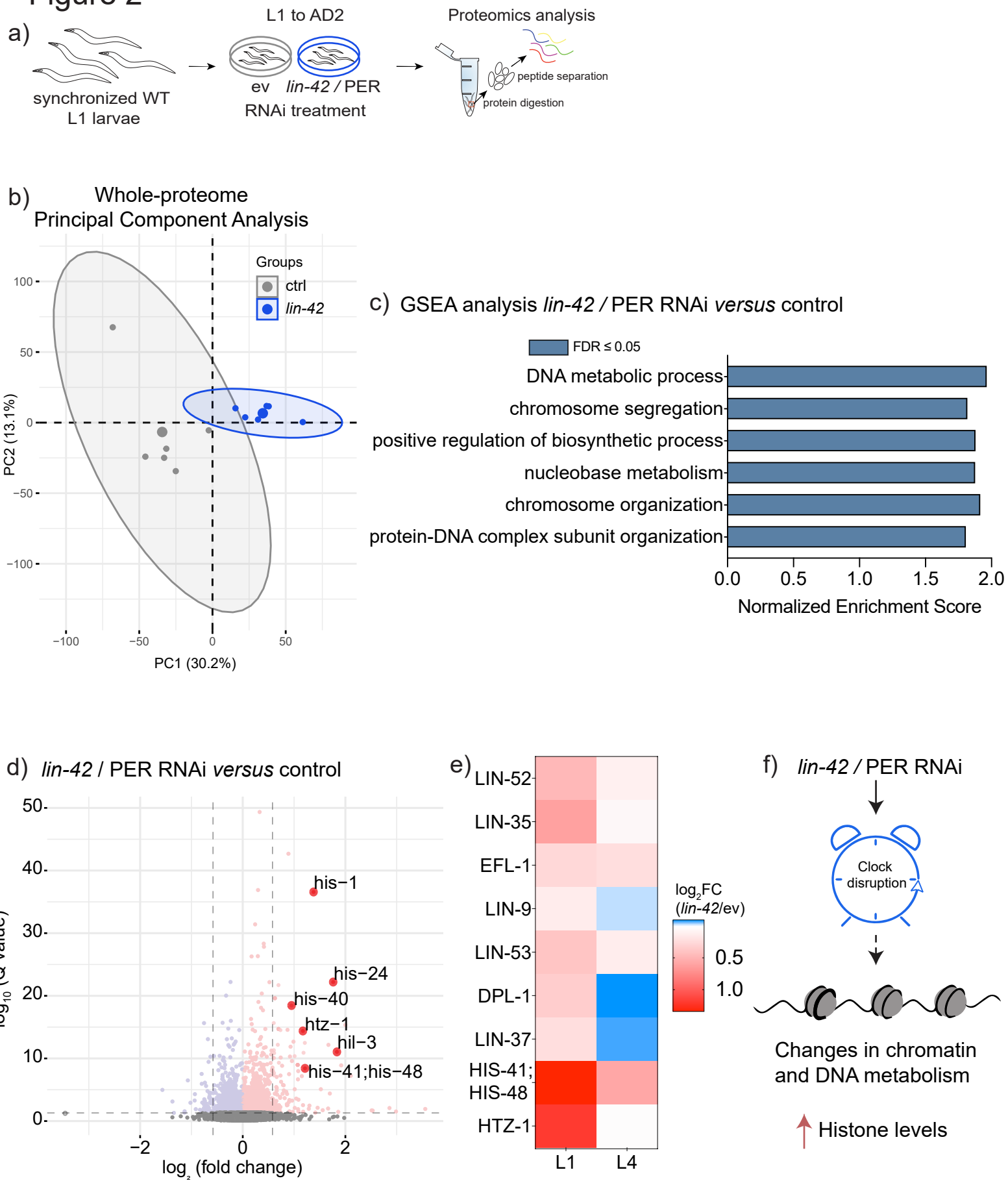
a)
synchronized WT
L1 larvae
L1 to AD2
ev
lin-42 / PER
RNAi treatment
Proteomics analysis
peptide separation
protein digestion
b)
Whole-proteome
Principal Component Analysis
Groups
ctrl
lin-42
PC2 (13.1%)
PC1 (30.2%)
c) GSEA analysis lin-42 / PER RNAi versus control
FDR ≤ 0.05
DNA metabolic process
chromosome segregation
positive regulation of biosynthetic process
nucleobase metabolism
chromosome organization
protein-DNA complex subunit organization
Normalized Enrichment Score
d) lin-42 / PER RNAi versus control
his−1
his−24
his−40
htz−1
hil−3
his−41;his−48
−log10 (Q value)
log2 (fold change)
e)
LIN-52
LIN-35
EFL-1
LIN-9
LIN-53
DPL-1
LIN-37
HIS-41;
HIS-48
HTZ-1
L1
L4
log2FC
(lin-42/ev)
0.5
1.0
f) lin-42 / PER RNAi
Clock
disruption
Changes in chromatin
and DNA metabolism
Histone levels

Figure 3

a)

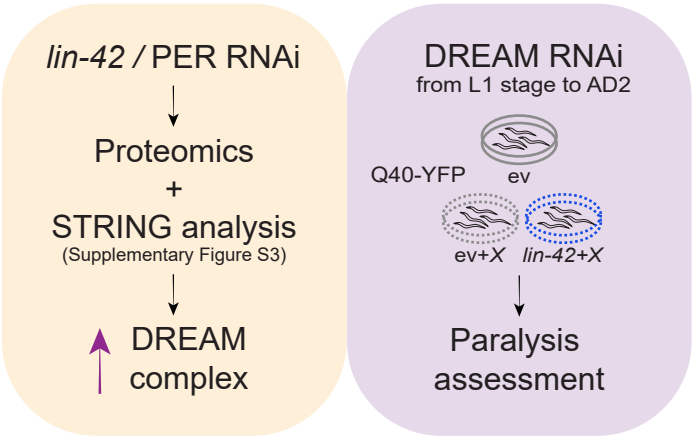

b)

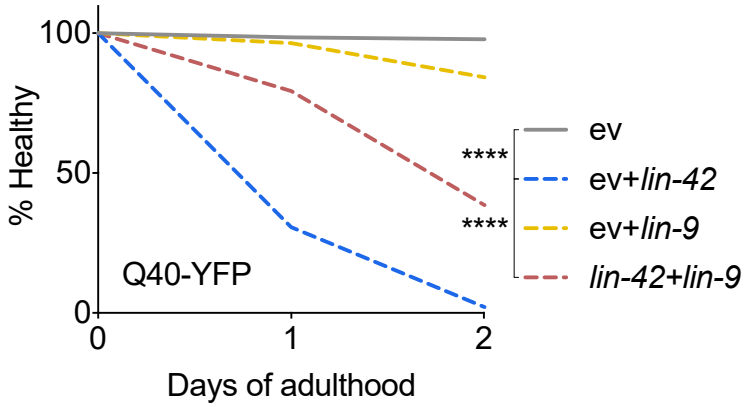

c)

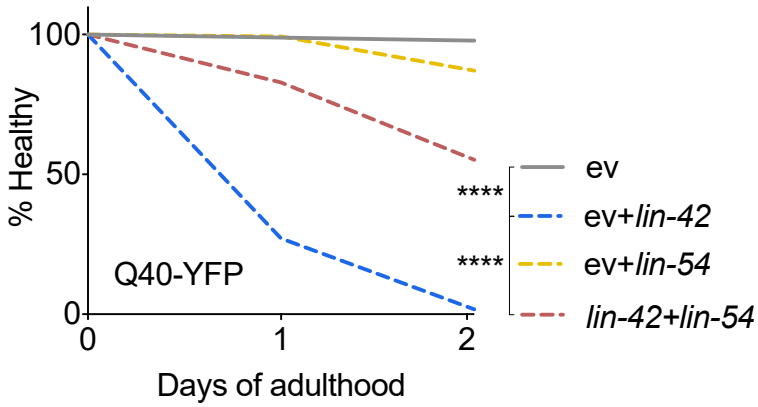

d)

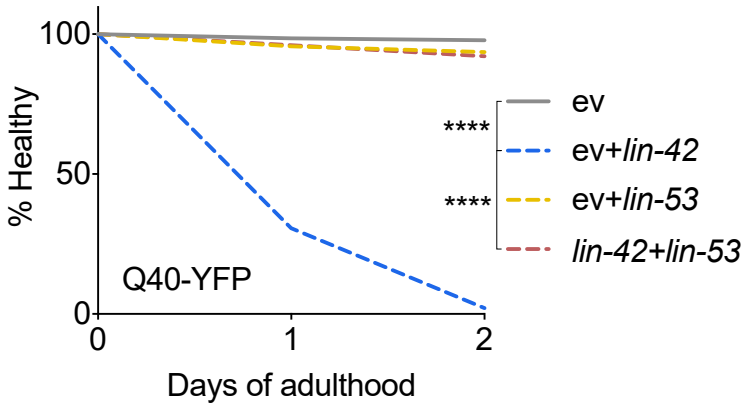

e)

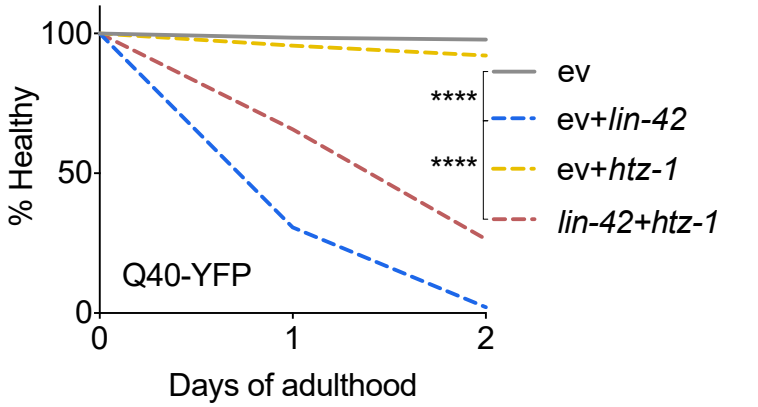

f)

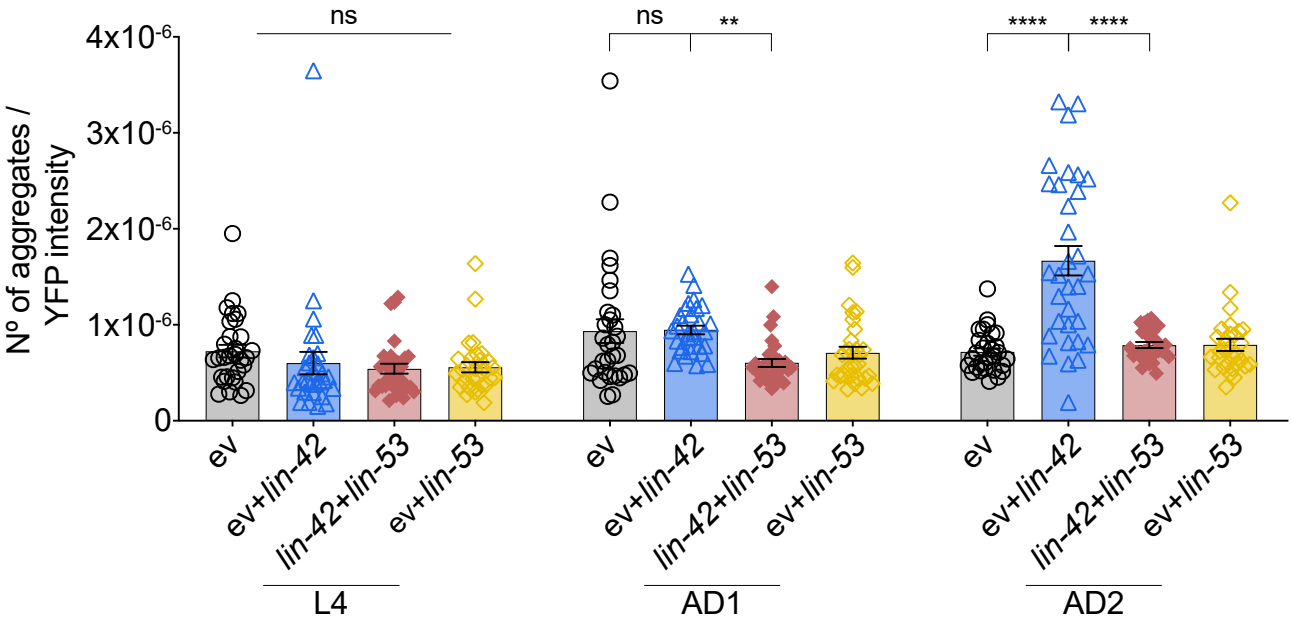

Figure 4

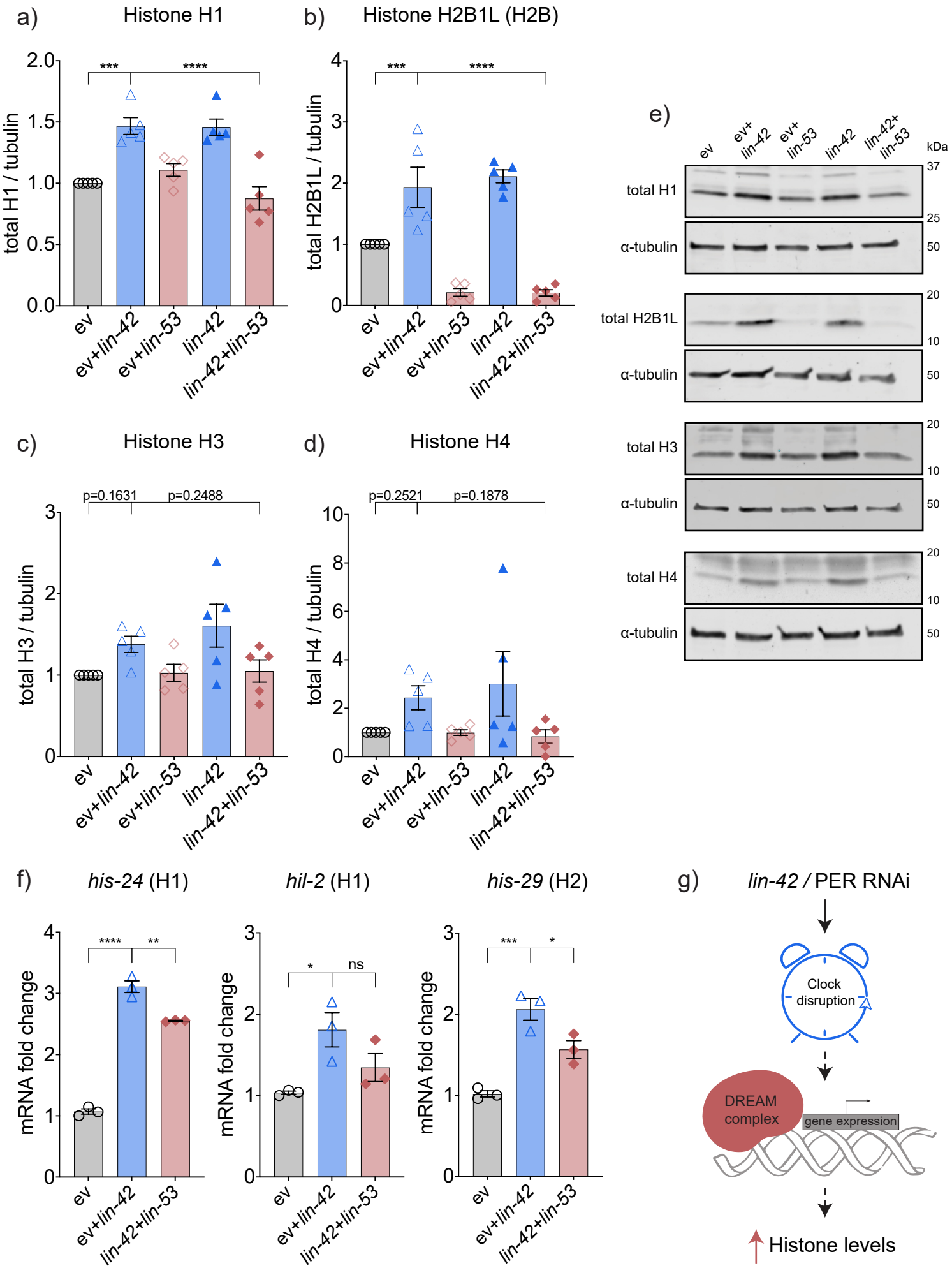
a)
Histone H1
total H1 / tubulin
***
****
ev
ev+lin-42
ev+lin-53
lin-42
lin-42+lin-53
b)
Histone H2B1L (H2B)
total H2B1L / tubulin
c)
Histone H3
total H3 / tubulin
p=0.1631
p=0.2488
d)
Histone H4
total H4 / tubulin
p=0.2521
p=0.1878
e)
ev
ev+ lin-42
ev+ lin-53
lin-42
lin-42+ lin-53
kDa
total H1
α-tubulin
total H2B1L
total H3
total H4
f)
his-24 (H1)
hil-2 (H1)
his-29 (H2)
mRNA fold change
**
*
ns
g)
lin-42 / PER RNAi
Clock disruption
DREAM complex
gene expression
Histone levels

Figure 5

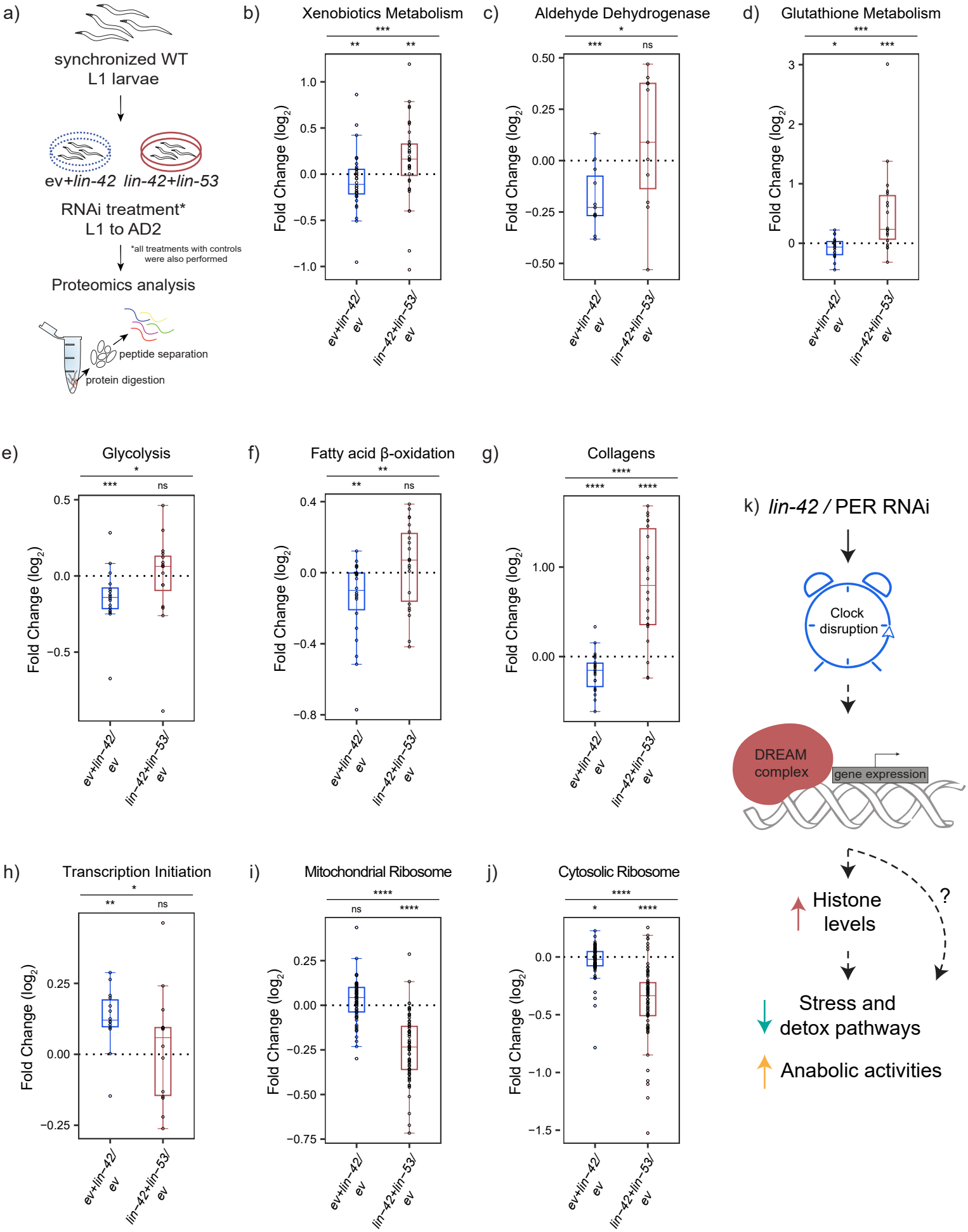
a)
synchronized WT
L1 larvae
ev+lin-42
lin-42+lin-53
RNAi treatment*
L1 to AD2
*all treatments with controls were also performed
Proteomics analysis
peptide separation
protein digestion
b)
Xenobiotics Metabolism
c)
Aldehyde Dehydrogenase
d)
Glutathione Metabolism
e)
Glycolysis
f)
Fatty acid β-oxidation
g)
Collagens
h)
Transcription Initiation
i)
Mitochondrial Ribosome
j)
Cytosolic Ribosome
Fold Change (log2)
ev+lin-42/ ev
lin-42+lin-53/ ev
k) lin-42 / PER RNAi
Clock disruption
DREAM complex
gene expression
Histone levels
?
Stress and detox pathways
Anabolic activities

Figure 6

mouse brain

a) Mitochondria ZT0

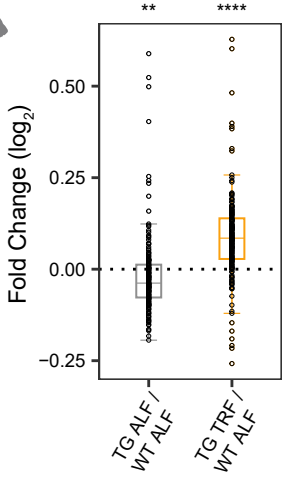

Mitochondria ZT12

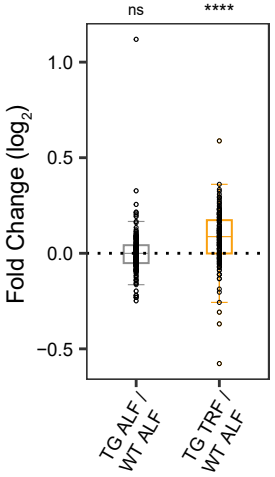

b) OXPHOS ZT0

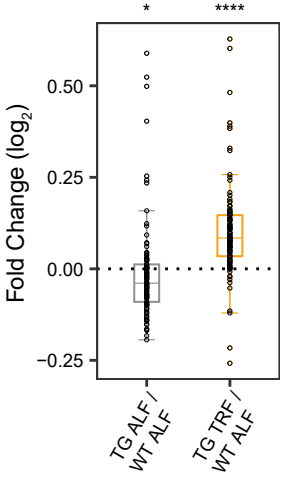

OXPHOS ZT12

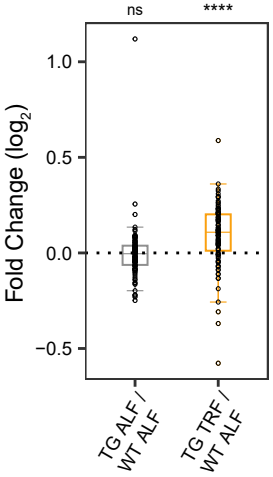

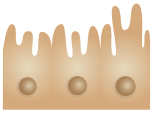

human RPE cells

c) PER1

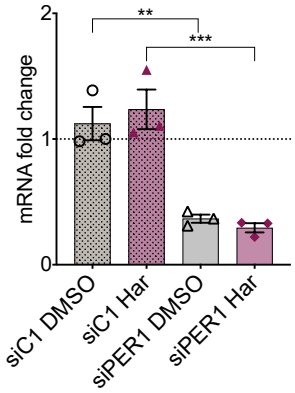

PER1

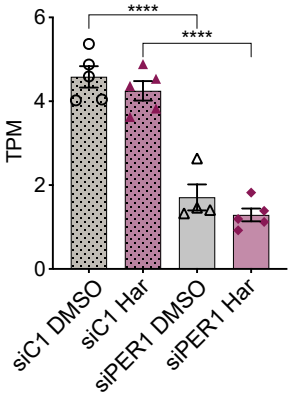

d) CLOCK

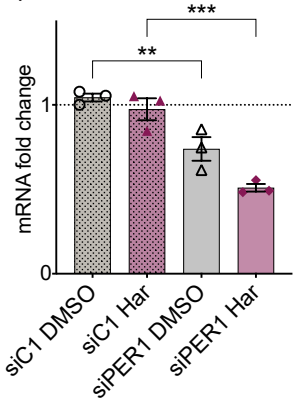

CLOCK

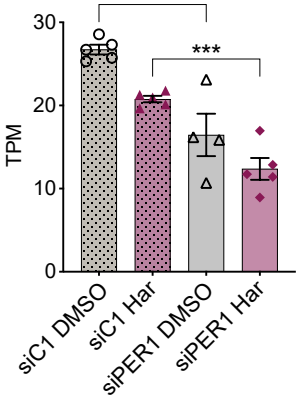

e) Mitochondria

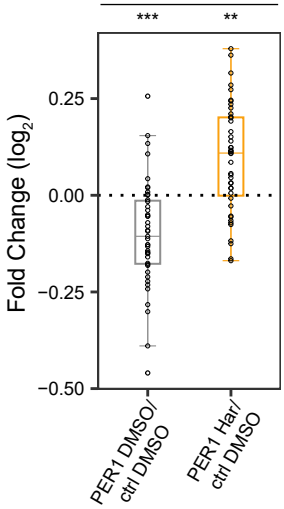

f) OXPHOS

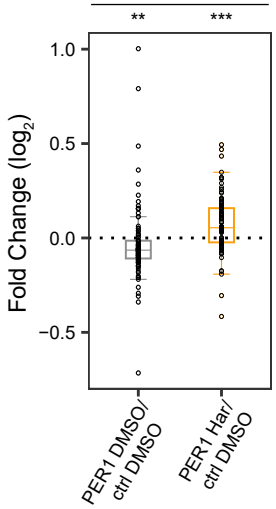

h) *lin-42* / PER RNAi

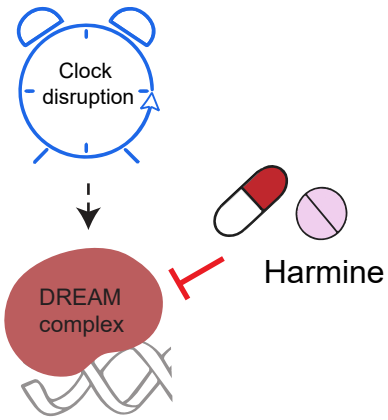

Abrogation of cellular maintenance pathways

Broad disruption of cellular health

C. elegans

g)

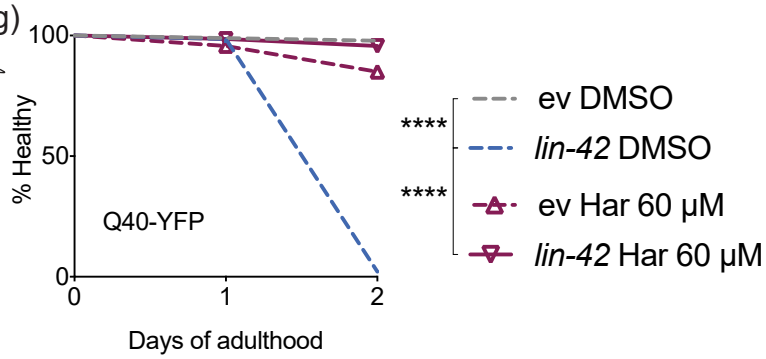

Figure S1

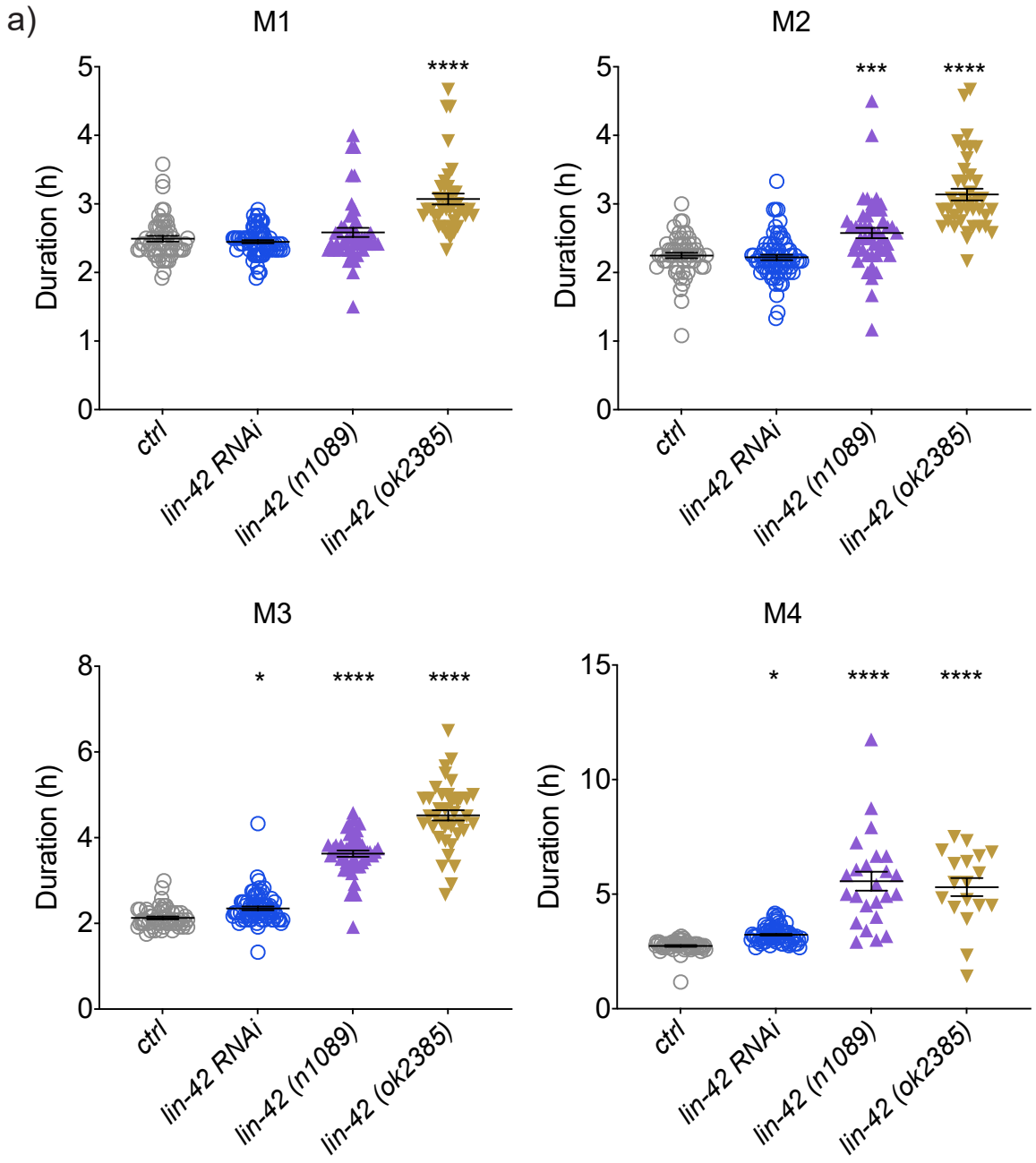
a)
M1
M2
M3
M4
Duration (h)
ctrl
lin-42 RNAi
lin-42 (n1089)
lin-42 (ok2385)
*
***
****

Figure S2

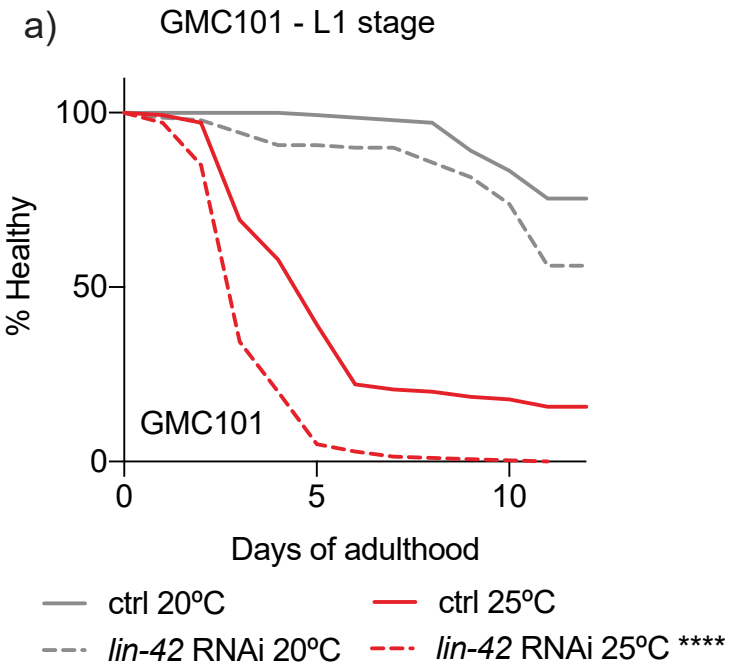
a)
GMC101 - L1 stage
100
50
0
% Healthy
GMC101
0
5
10
Days of adulthood
ctrl 20ºC
ctrl 25ºC
lin-42 RNAi 20ºC
lin-42 RNAi 25ºC ****

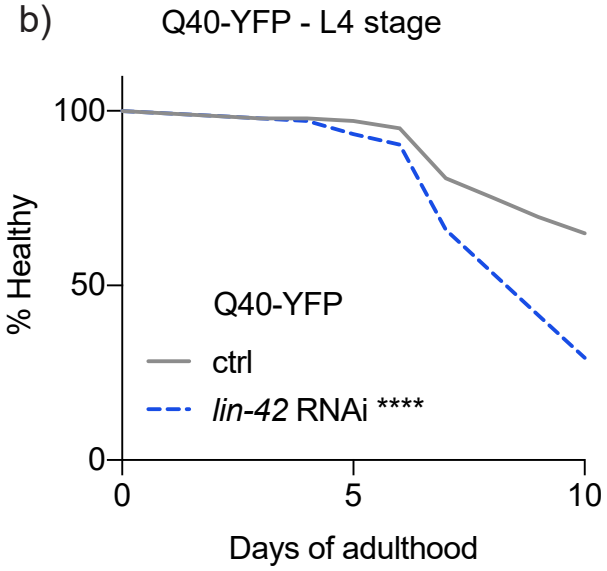
b)
Q40-YFP - L4 stage
100
50
0
% Healthy
Q40-YFP
ctrl
lin-42 RNAi ****
0
5
10
Days of adulthood

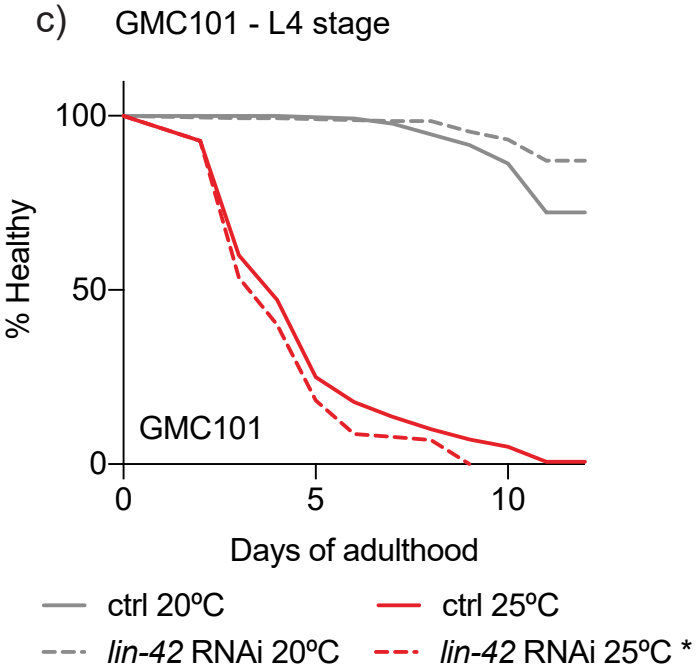
c)
GMC101 - L4 stage
100
50
0
% Healthy
GMC101
0
5
10
Days of adulthood
ctrl 20ºC
ctrl 25ºC
lin-42 RNAi 20ºC
lin-42 RNAi 25ºC *

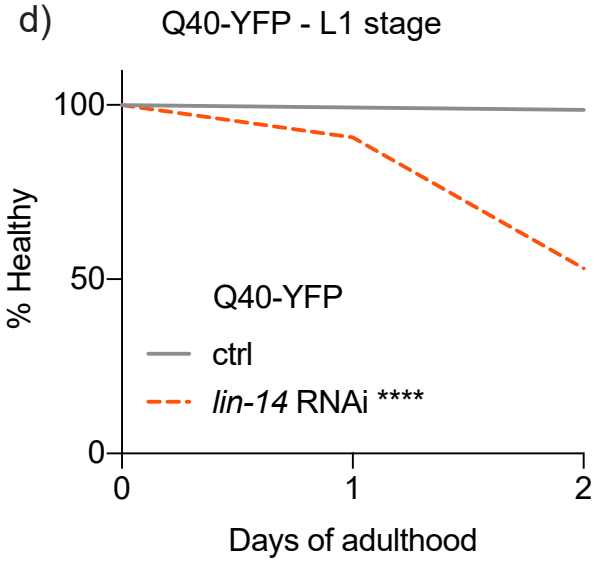
d)
Q40-YFP - L1 stage
100
50
0
% Healthy
Q40-YFP
ctrl
lin-14 RNAi ****
0
1
2
Days of adulthood

Figure S3

a)

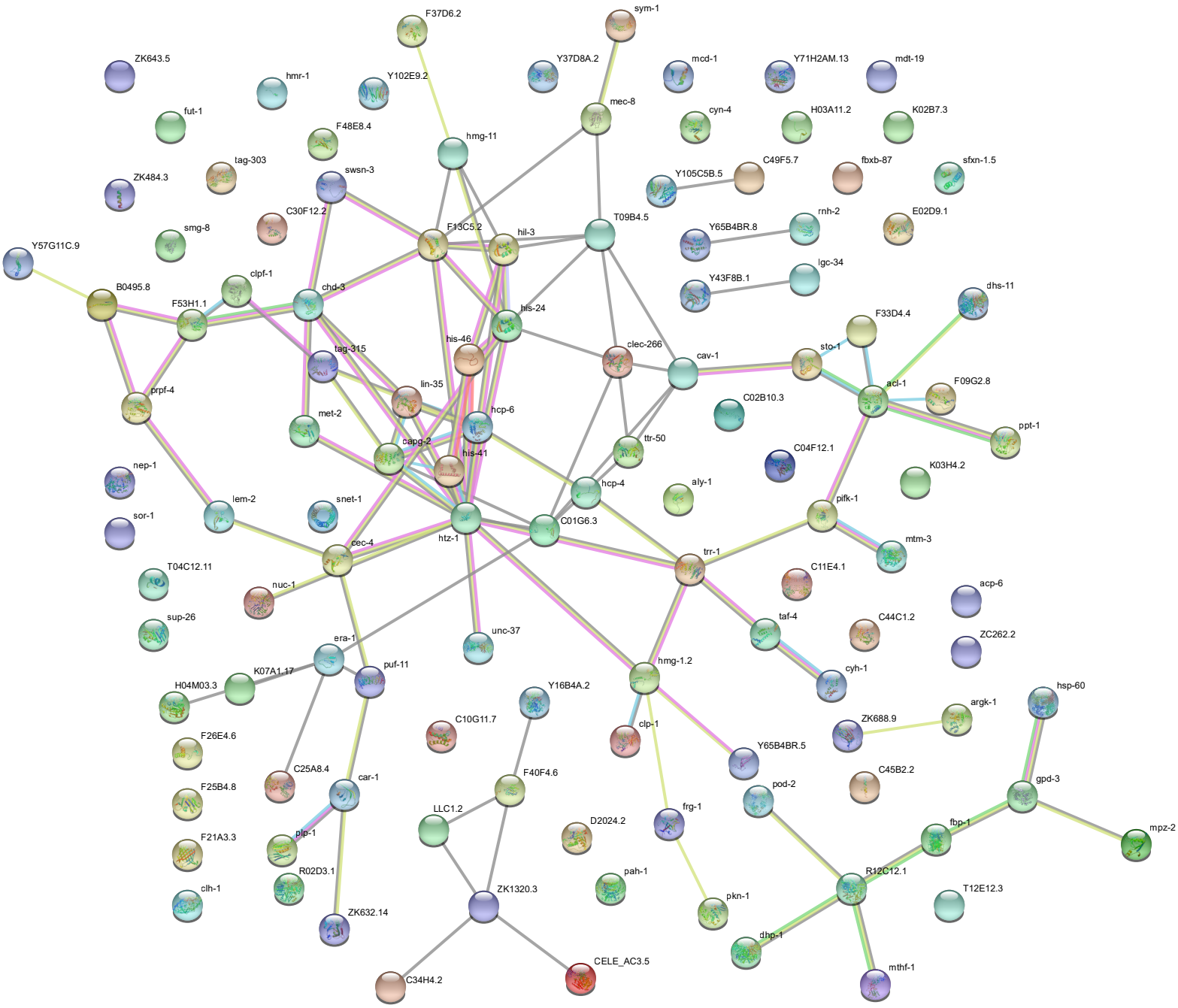
F37D6.2
sym-1
ZK643.5
hmr-1
Y102E9.2
Y37D8A.2
mcd-1
Y71H2AM.13
mdt-19
fut-1
F48E8.4
hmg-11
mec-8
cyn-4
H03A11.2
K02B7.3
tag-303
swsn-3
ZK484.3
Y105C5B.5
C49F5.7
fbxb-87
sfxn-1.5
C30F12.2
smg-8
F13C5.2
hil-3
T09B4.5
Y65B4BR.8
rnh-2
E02D9.1
Y57G11C.9
clpf-1
chd-3
Y43F8B.1
lgc-34
B0495.8
F53H1.1
his-24
dhs-11
F33D4.4
his-46
tag-315
clec-266
cav-1
sto-1
lin-35
acl-1
F09G2.8
prpf-4
met-2
hcp-6
C02B10.3
ppt-1
capg-2
ttr-50
C04F12.1
nep-1
his-41
K03H4.2
hcp-4
aly-1
lem-2
snet-1
pifk-1
sor-1
htz-1
C01G6.3
mtm-3
cec-4
trr-1
T04C12.11
C11E4.1
nuc-1
acp-6
sup-26
taf-4
C44C1.2
unc-37
ZC262.2
era-1
hmg-1.2
cyh-1
K07A1.17
puf-11
H04M03.3
Y16B4A.2
hsp-60
argk-1
C10G11.7
clp-1
ZK688.9
F26E4.6
Y65B4BR.5
C25A8.4
car-1
F40F4.6
C45B2.2
F25B4.8
pod-2
gpd-3
LLC1.2
frg-1
D2024.2
fbp-1
mpz-2
F21A3.3
plp-1
R02D3.1
pah-1
R12C12.1
clh-1
ZK1320.3
pkn-1
T12E12.3
ZK632.14
dhp-1
CELE_AC3.5
mthf-1
C34H4.2

Figure S4

a)

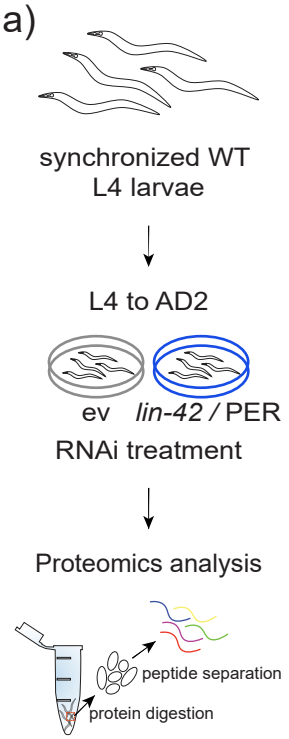

b) Whole-proteome - Principal Component Analysis

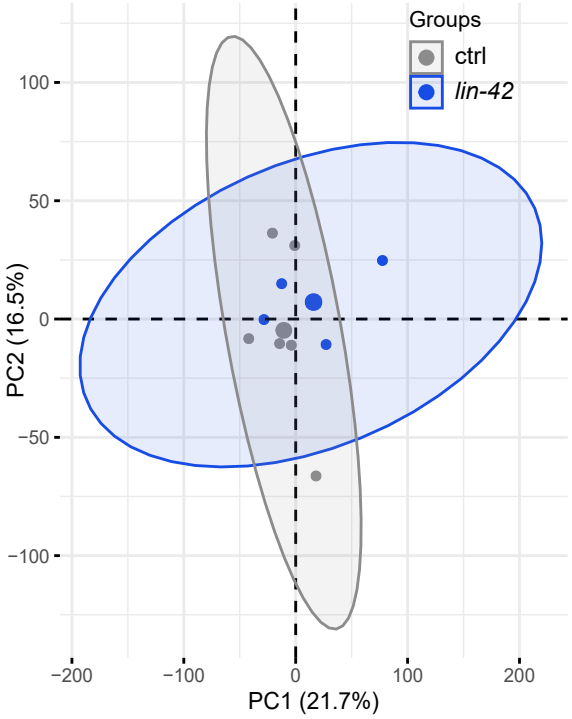

c)

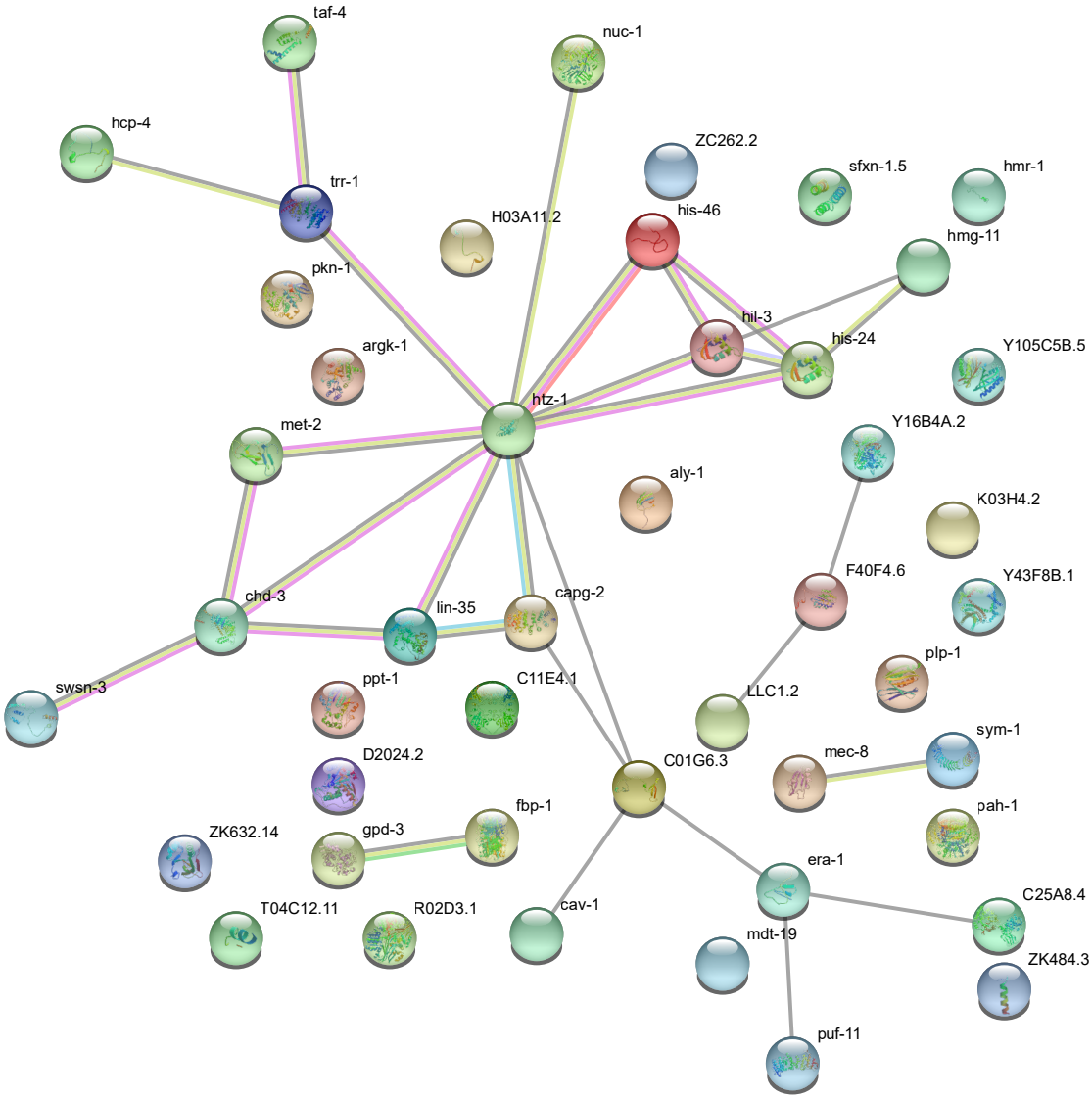

Figure S5

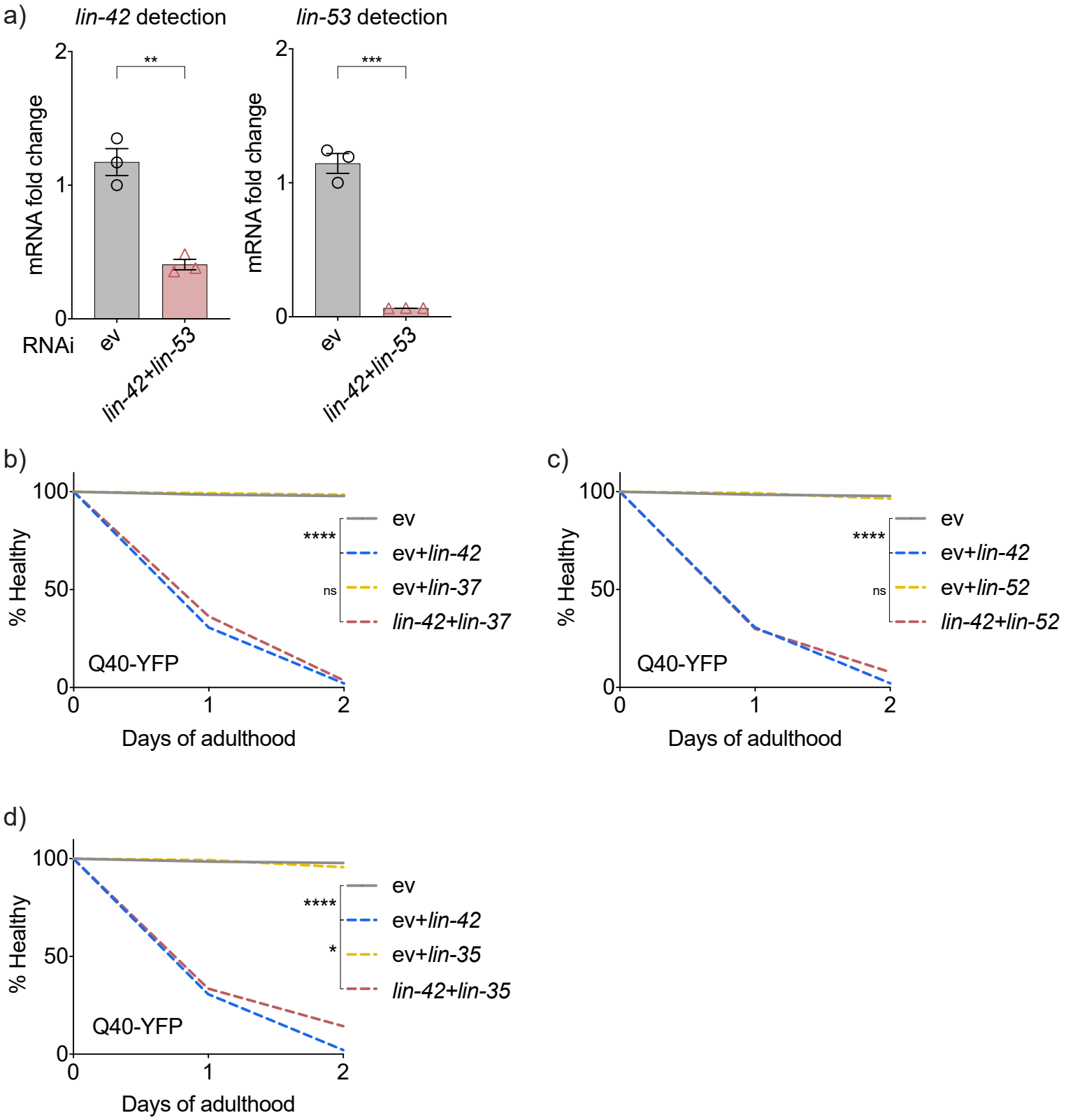
a)
lin-42 detection
lin-53 detection
mRNA fold change
**
***
RNAi
ev
lin-42+lin-53
b)
% Healthy
Days of adulthood
Q40-YFP
****
ns
ev
ev+lin-42
ev+lin-37
lin-42+lin-37
c)
ev+lin-52
lin-42+lin-52
d)
*
ev+lin-35
lin-42+lin-35

Figure S6

a)

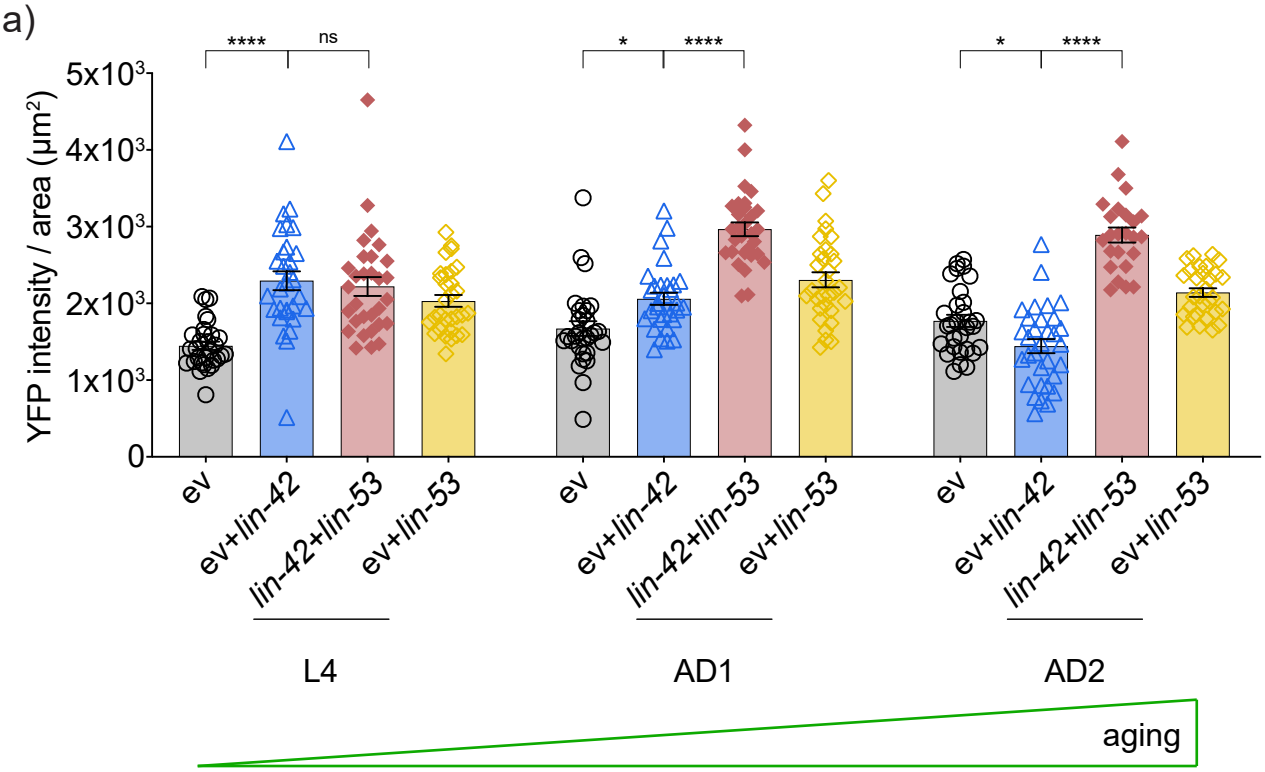

b) Q40-YFP

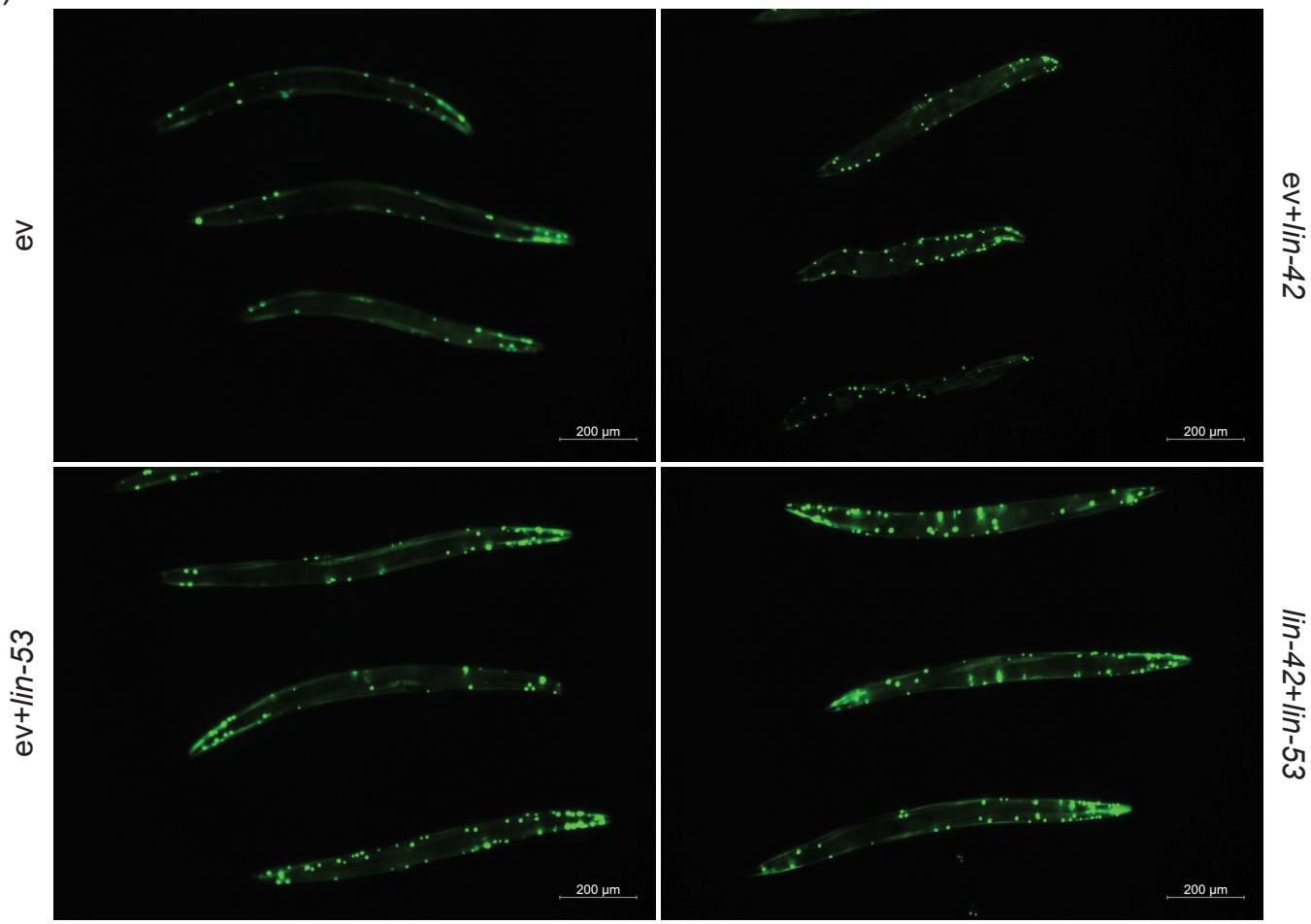

Figure S7

a) Histone H1

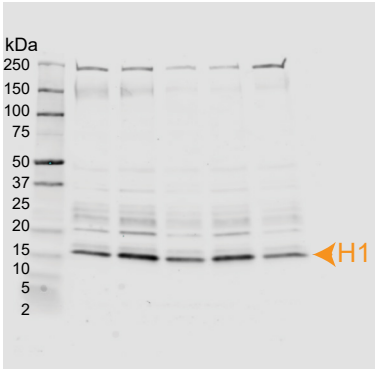

α-Tubulin

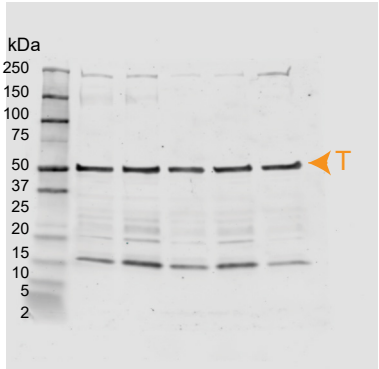

b) Histone H2B1L

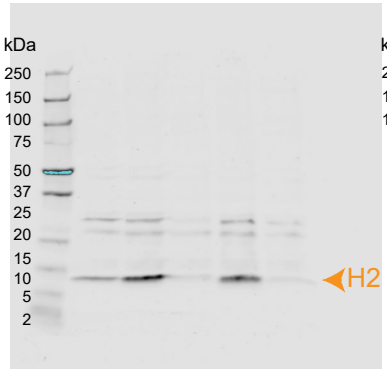

α-Tubulin

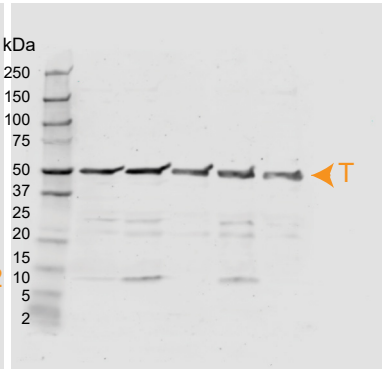

c) Histone H3
α-Tubulin

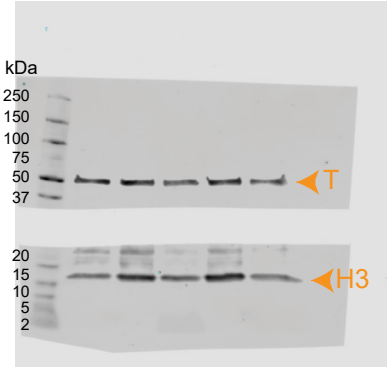

d) Histone H4

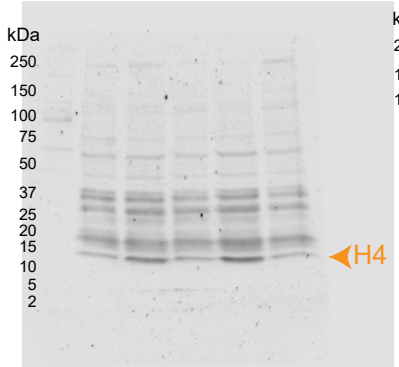

α-Tubulin

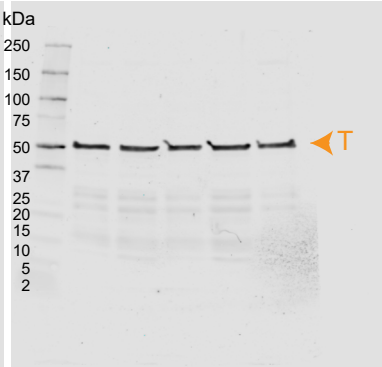

Figure S8

a)

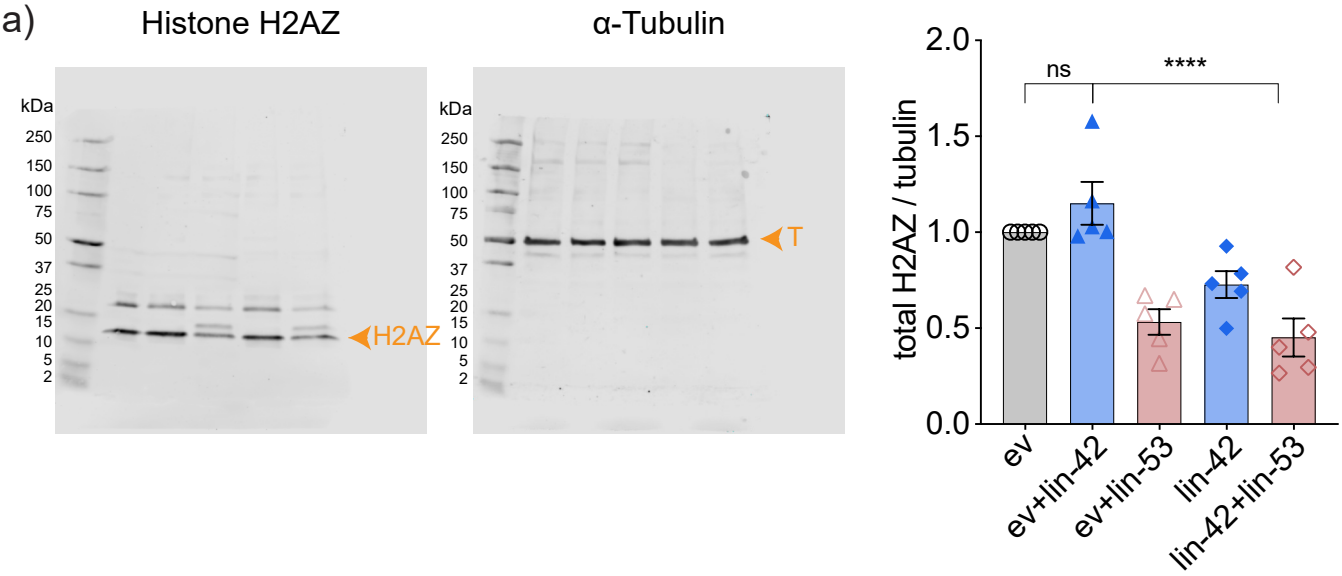
Histone H2AZ
α-Tubulin
kDa
250
150
100
75
50
37
25
20
15
10
5
2
H2AZ
T
total H2AZ / tubulin
2.0
1.5
1.0
0.5
0.0
ns
****
ev
ev+lin-42
ev+lin-53
lin-42
lin-42+lin-53

Figure S9

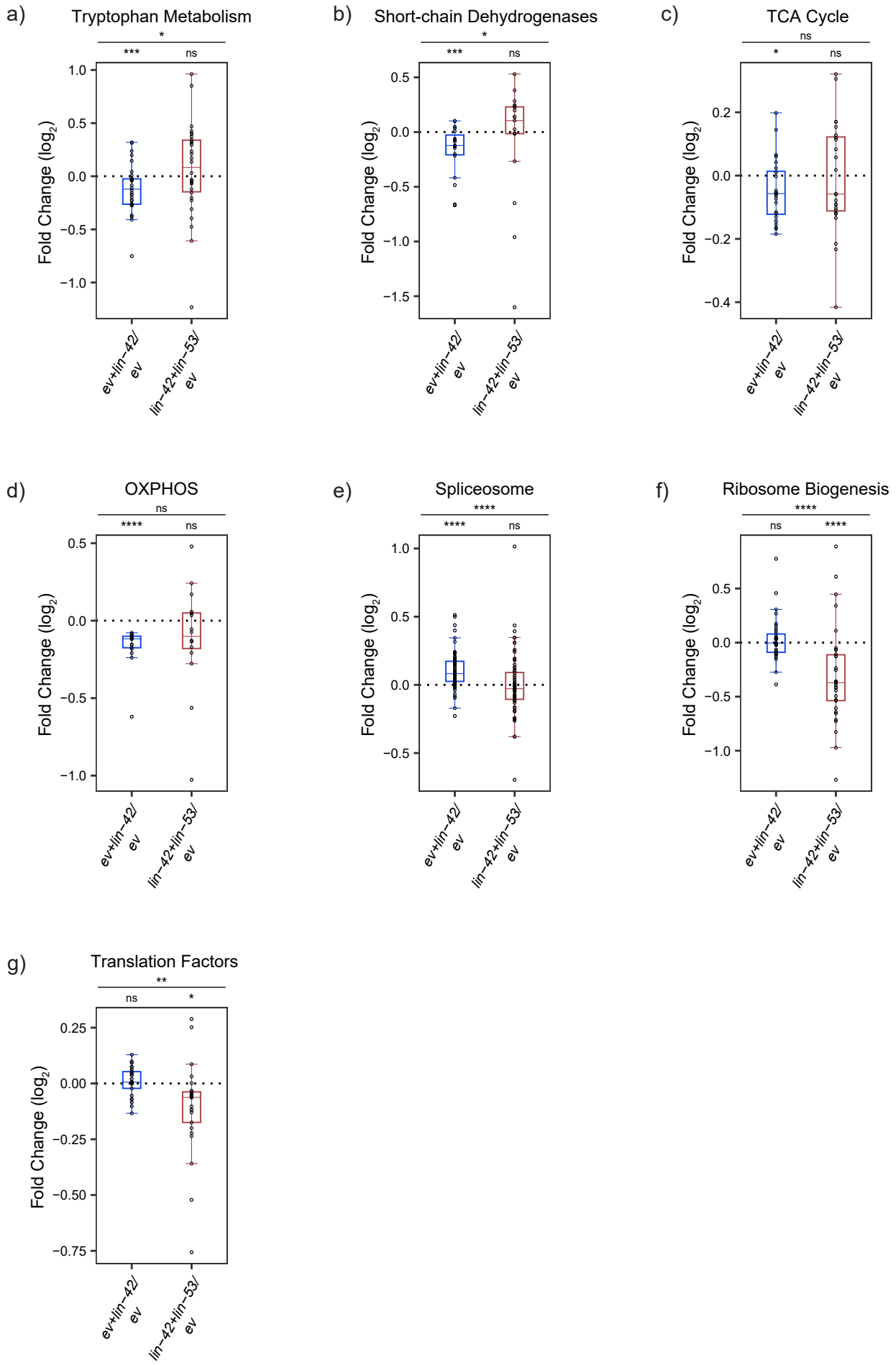
a)
Tryptophan Metabolism
*
***
ns
Fold Change (log2)
1.0
0.5
0.0
−0.5
−1.0
ev+lin−42/ ev
lin−42+lin−53/ ev
b)
Short-chain Dehydrogenases
*
***
ns
Fold Change (log2)
0.5
0.0
−0.5
−1.0
−1.5
ev+lin−42/ ev
lin−42+lin−53/ ev
c)
TCA Cycle
ns
*
ns
Fold Change (log2)
0.2
0.0
−0.2
−0.4
ev+lin−42/ ev
lin−42+lin−53/ ev
d)
OXPHOS
ns
****
ns
Fold Change (log2)
0.5
0.0
−0.5
−1.0
ev+lin−42/ ev
lin−42+lin−53/ ev
e)
Spliceosome
****
****
ns
Fold Change (log2)
1.0
0.5
0.0
−0.5
ev+lin−42/ ev
lin−42+lin−53/ ev
f)
Ribosome Biogenesis
****
ns
****
Fold Change (log2)
0.5
0.0
−0.5
−1.0
ev+lin−42/ ev
lin−42+lin−53/ ev
g)
Translation Factors
**
ns
*
Fold Change (log2)
0.25
0.00
−0.25
−0.50
−0.75
ev+lin−42/ ev
lin−42+lin−53/ ev

Figure S10

a)

mouse brain

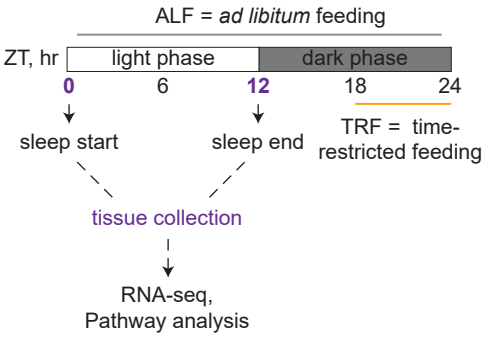

b)

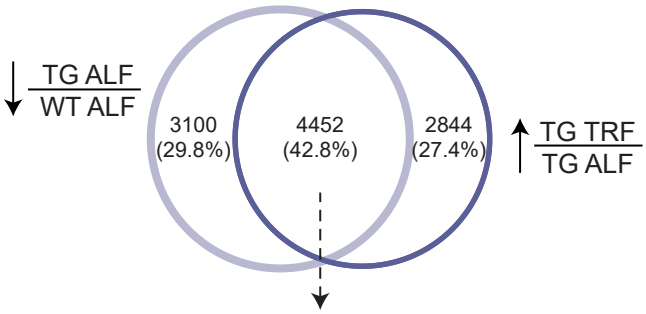

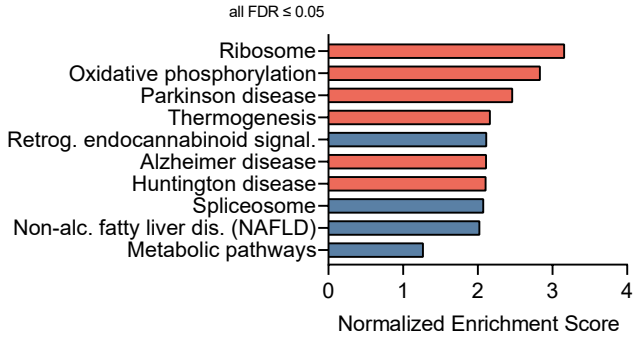

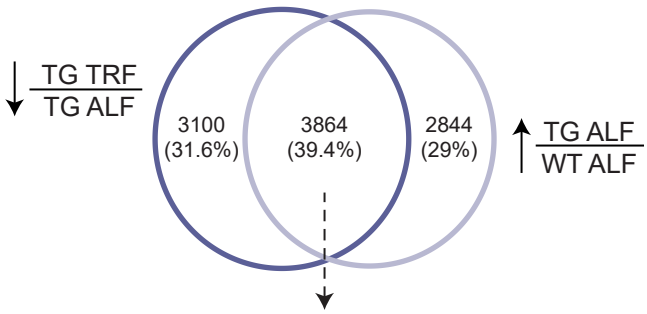

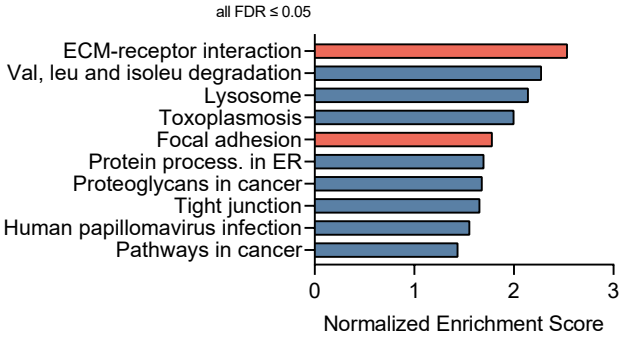

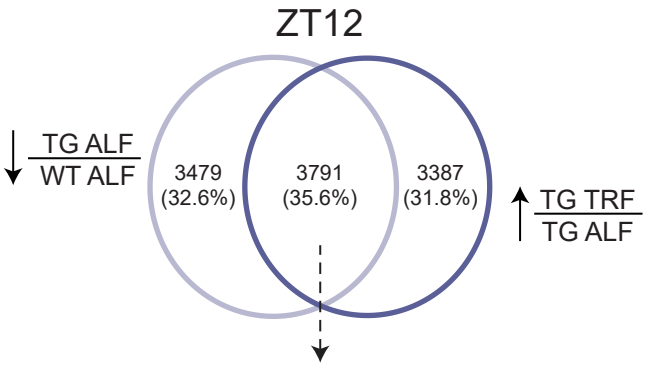

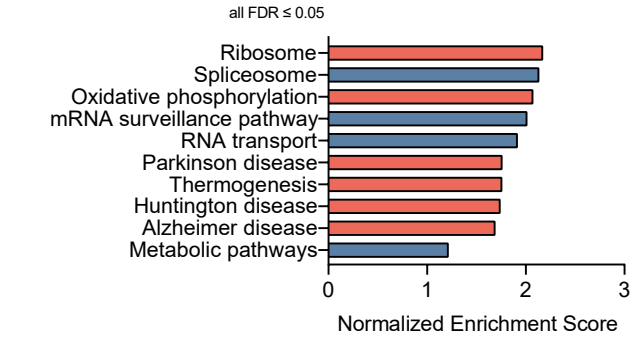

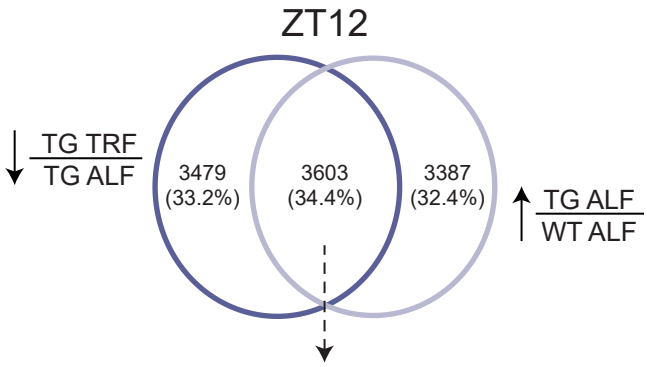

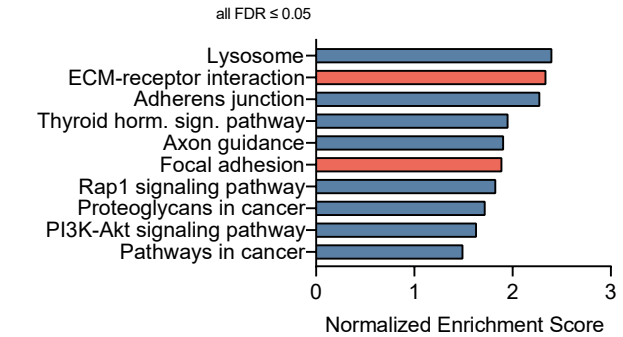

Figure S11

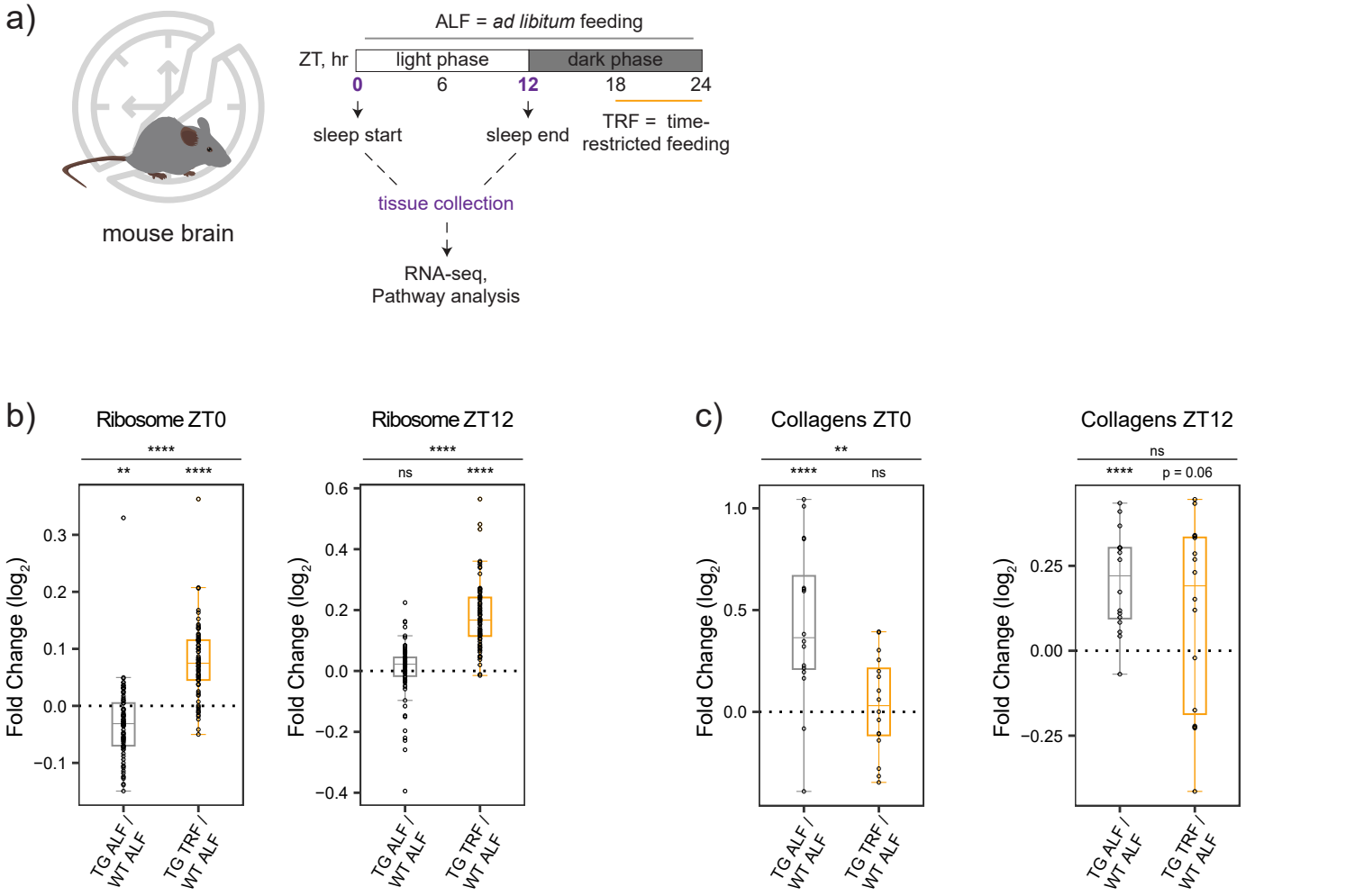
a)
mouse brain
ALF = ad libitum feeding
ZT, hr
light phase
dark phase
0
6
12
18
24
sleep start
sleep end
TRF = time-restricted feeding
tissue collection
RNA-seq, Pathway analysis
b)
Ribosome ZT0
Ribosome ZT12
c)
Collagens ZT0
Collagens ZT12
Fold Change (log2)
TG ALF / WT ALF
TG TRF / WT ALF
ns
p = 0.06

Figure S12

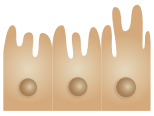

human RPE cells

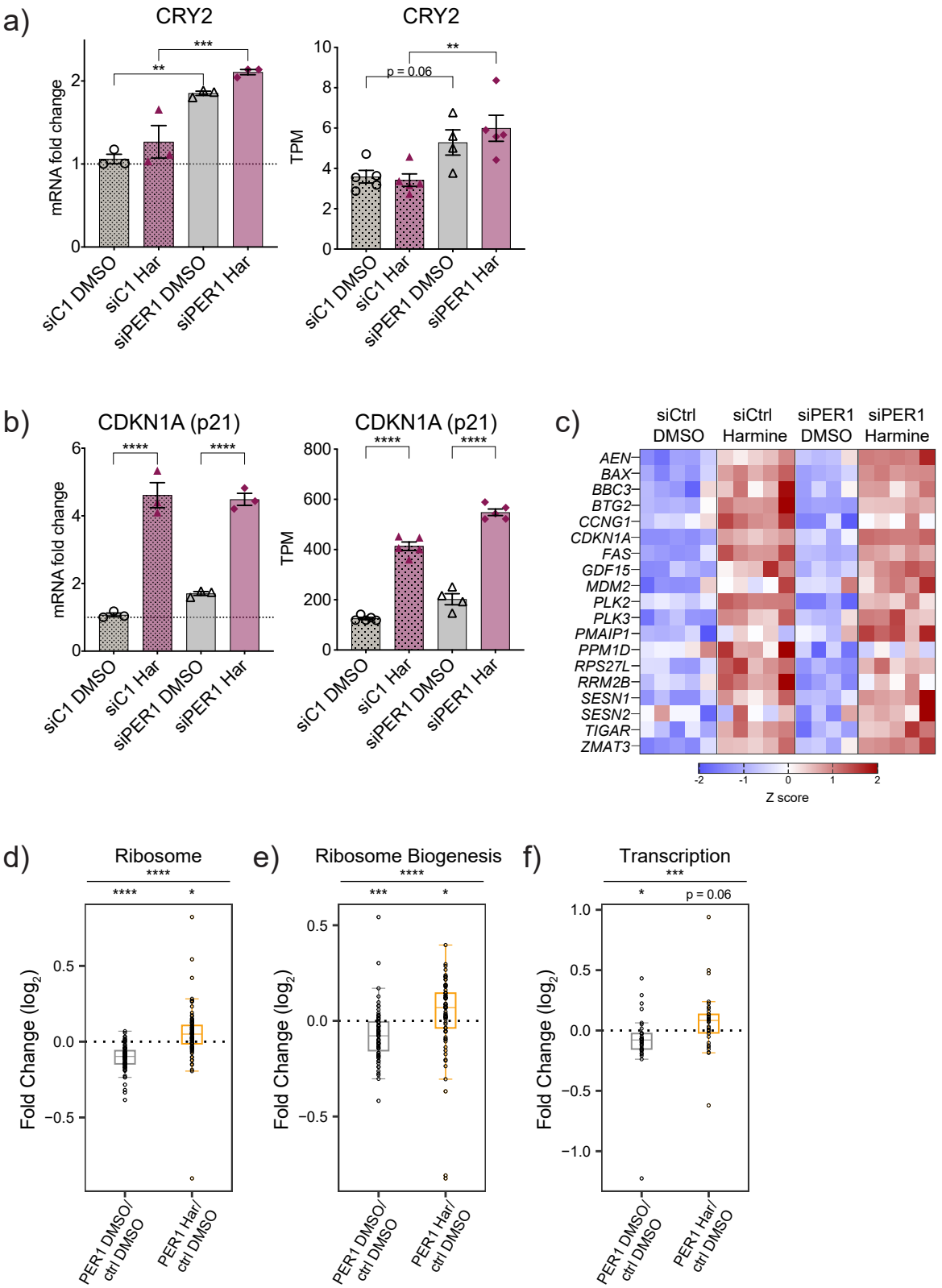

C. elegans

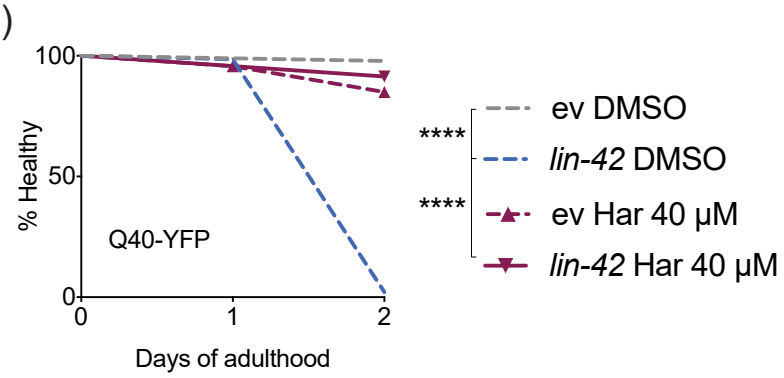

Figure S13

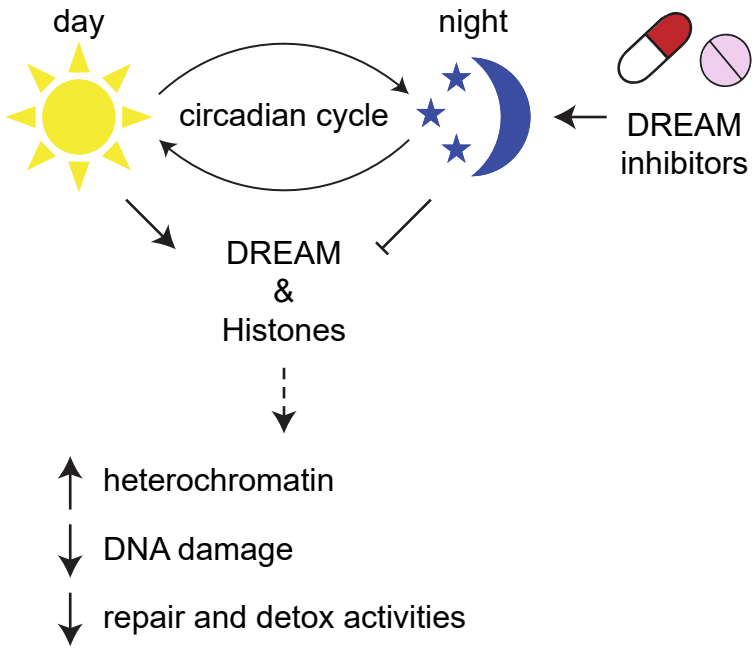
day
night
circadian cycle
DREAM
inhibitors
DREAM
&
Histones
heterochromatin
DNA damage
repair and detox activities

Materials and methods.

C. elegans strains

The following *C. elegans* strains were used in this study: N2 (*C. elegans* Bristol wild-type isolate), GMC101 *dvls100 [unc-54p::Aβ$_{1-42}$::unc-54 3'UTR+ mtl-2p::GFP]*, AM141 *rmls133 [unc-54p::Q40::YFP]*, MT2257 *lin-42(n1089)* II, RB1843 *lin-42(ok2385) II*, MRS 387 *sevIs1* [Psur-5::luc+::gfp], MOL459 *lin-42(n1089)* II; sevIs1[Psur-5::luc+::gfp], MOL460 (*lin-42(ok2385)* II; *sevIs1*[Psur-5::luc+::gfp]) YZ. GMC101, AM141, MT2257 and RB1843 strains were obtained from the Caenorhabditis Genetics Center (CGC, University of Minnesota). Luminometry strains were generated as described in[1] and crossed to MT2257 and RB1843 strains. All strains were maintained under standard laboratory conditions as described in[2].

Bacterial strains and experimental conditions

E. coli OP50 and *E. coli* HT115(DE3) were seeded on lysogeny broth (LB) agar plates and kept at 4ºC. OP50 cultures were grown overnight in LB medium without antibiotics and were used on standard nematode growth medium (NGM) agar for maintenance of all *C. elegans* strains. For RNAi experiments, HT115 bacteria expressing the specific dsRNA construct were obtained from ORF and Ahringer libraries (Source Biosciences, Nottingham, UK). All RNAi bacteria were grown in LB agar plates supplemented with ampicillin (100 mg/mL) and tetracycline (12.5 mg/mL) (Roth, #K029.1 and #0237.1). Plates were kept at 4ºC, and overnight cultures were grown in an LB medium containing ampicillin. RNAi expression was induced by adding 1 mM isopropylthiogalactoside (IPTG, Sigma, #16758) and incubating the cultures at 37ºC for 25 min before seeding bacteria on NGM agar supplemented with ampicillin and 3 mM IPTG. For double RNAi experiments, the OD of each culture was measured at 590 nm (Tecan, Männedorf, Switzerland) and mixed in a 1:1 ratio. Harmine (Sigma-Aldrich, SMB00461) was dissolved in DMSO and given in NGM agar in combination with ampicillin and IPTG.

Bacterial sequencing

Plasmid DNA of RNAi bacteria was isolated using an innuPREP plasmid mini kit (Analytik Jena, Jena, Germany) and following the manufacturer's instructions. pDNA concentration was measured by Nanodrop (Thermo Fisher Scientific, Bremen, Germany). 50-100 ng/ µL pDNA was sent together with forward and reverse primers at 10 mM (L4440 forward: 5'-GTTTTCCCAGTCACGACGTT-3', L4440 reverse: 5'-TGGATAACCGTATTACCGCC-3') to Eurofins Genomics (Ebersberg, Germany). RNAi hit location was verified by the Basic Local Alignment Search Tool (BLAST, Wormbase).

Luminometry assay

We measured the duration of intermolts and molts by using a luminescence-based method[3]. To obtain synchronized eggs, 10-12 gravid hermaphrodites were transferred to fresh NGM plates to lay eggs for 1 hour. Using an eyelash, embryos were individually transferred to wells of a 96-well plate, each well containing 100 µl of S-basal (10 µg/ml cholesterol) with 200 µM Luciferin, 2 mM IPTG and 200 µg/ml Ampicillin. As food source, we added 100 µl of S-Basal containing 20 g/l bacteria containing the pL4440 empty vector for the control *(ctrl), lin-42 (n1089)* and *lin-42 (ok2385)* conditions, or with bacteria expressing RNAi against *lin-42* (*lin-42 RNAi*). To obtain the 20 g/l bacterial food source, the bacterial strains were cultured in LB medium containing 100 mg/ml Ampicilin and 12.5 mg/ml Tetracycline o/n at 37 ºC, in constant shaking. The next day, the cultures were diluted 1:10 in fresh LB (with Ampicilin and Tetracycline) and incubated for 3 hours in the same conditions. After that, 1 mM IPTG was added and cultured for another 2 hours. To finally obtain the 20 g/l concentration, the bacterial cultures were centrifugated and resuspended in S-Basal twice, then adjusted the bacteria concentration was adjusted to 20 g/l. After addition of the bacteria, the plates were sealed using a gas-permeable membrane. The plate was introduced in the luminometry reader (Berthold Centro XS3), placed inside a cooled incubator (Panasonic MIR-254) set at 16.5 ºC, to allow a temperature on the plate of 20 ºC. We measured luminesce for 1 sec at 5-min intervals, until animals reached adulthood. We analysed luminometry data as previously described[3].

Lifespan analysis

N2 worms were cultivated in RNAi plates and fed with bacteria expressing RNAi against *lin-42* or harboring the empty vector (ev) control construct. Specific RNAi exposure was initiated at two different time points: i) from the L1 stage or ii) from the L4 stage. For group ii, the

worms were grown in ev plates from L1 stage and until the start of *lin-42* RNAi exposure. For each lifespan condition, two plates of 70 worms were used. The viability was accessed daily by using SteREO Discovery.V8 microscope (Carl Zeiss Microscopy, Jena, Germany), and the worms were transferred to new freshly seeded plates every 2 days until adulthood day 10 (AD10), and every 4 days thereafter. Every worm that showed no touch response was considered dead. Internal hatching, gut explosions and escaping worms were censored.

GMC101 paralysis tests

Paralysis was evaluated as previously reported[4]. *lin-42* RNAi exposure was initiated at two time points i) L1 stage or ii) L4 stage. For group ii, the animals were grown on ev expressing bacteria from L1 and until the L4 stage. Two plates of 70 worms were used for each condition. All plates were kept at 20ºC until the L4 stage, and afterwards half was shifted to 25ºC to trigger Aβ toxicity. Paralysis was scored daily using SteREO Discovery.V8 microscope (Carl Zeiss Microscopy, Jena, Germany). Immobile worms insensitive to touch were considered paralyzed. Worms were transferred to new freshly seeded plates every second day until AD10, and every fourth day thereafter.

AM141 paralysis tests

Paralysis was evaluated as previously reported[5]. *lin-42* RNAi exposure was initiated at two time points i) L1 stage, ii) L4 stage. For group ii, the animals were grown on ev expressing bacteria from L1 and until the L4 stage. Two plates of 70 worms were analyzed for each condition. Paralysis was observed using SteREO Discovery.V8 microscope (Carl Zeiss Microscopy, Jena, Germany). Immobile worms insensitive to touch were considered paralyzed. Worms were transferred to new freshly seeded plates every second day until AD10, and every fourth day thereafter.

Proteomics sample collection, data acquisition and analysis.

Age-synchronized populations of N2 (wild type) worms were exposed to specific RNAis and their combinations i) from the L1 stage and ii) from the L4 stage and collected at adulthood day 2 (AD2); 800 worms per condition were collected. For group ii, worms were grown on ev RNAi from L1 stage and until L4 stage. Sample, preparation, data acquisition and data analysis

(DIA mode) were performed as described in detail previously[2]. The data (candidate table) and data reports (protein quantities) were exported, and further data analyses and visualization were performed with Rstudio using in-house pipelines and scripts.

Fluorescence microscopy

AM141 (Q40-YFP) animals treated as described in the figures were imaged at L4, AD1, and AD2 stages using Axio Zoom.V16 microscope fitted with PlanApo Z 0.5x objective (Carl Zeiss Microscopy, Jena, Germany). Fixed exposure times of 150 ms and 4.8 ms were used for YFP and brightfield imaging respectively, and 90x magnification was applied. Worms were immobilized by placement on ice for 30 min prior to microscopy, and 2 plates of 15 animals were scored for each condition. Image analysis was carried out using Zen software v2.6, blue edition (Carl Zeiss Microscopy, Jena, Germany). The area (body size, head to tail), YFP intensity and number of aggregates were measured for each animal, and following calculations were made: YFP intensity/area and number of aggregates/YFP intensity.

Western blotting

800 AD2 stage N2 worms per condition were harvested in 1xM9, followed by extraction with the lysis buffer (100 mM Hepes pH 8.5, 100 mM DTT, 1 mM EDTA, 1% SDS, 1 mM PMSF, 1x Protease inhibitor cocktail (Roche, #04693116001)) and homogenized by using Precellys 24 device and tubes (Precellys, Bertin Technologies, France). Four homogenization cycles (20 sec at 6.000 rpm) were applied separated by a 30-sec interval. The samples were centrifuged at 2500 rpm for 30 sec into a 1.5 mL tube, then sonicated (Bioruptor Plus, Diagenode, Belgium) for 10 cycles (60 sec ON/ 30 sec OFF) at a high setting and at 20°C. After sonication, samples were boiled at 95ºC for 5 min and centrifuged at 10600 rpm for 10 min.

Protein content was quantified using the EZQ Protein Quantitation Kit (Molecular Probes, Thermo Fisher Scientific, #R33200). Then, 20 ug protein was separated in 4-20% Mini-Protean TGX Precast Gels (Bio-Rad, California, US, #4561094) and blotted using Bio-Rad Trans-Blot Turbo device (Bio-Rad, California, US) onto a Nitrocellulose membrane 0.2 µm (Bio-Rad, California, US) for 30 min. Proteins were visualized with Ponceau S staining before incubation with 5% BSA (AppliChem, Darmstadt, Germany) in TBST for 1h at room temperature. Membranes were then incubated with primary antibodies in 5% BSA in TBST overnight at 4ºC. The following primary antibodies were used: total histone H1 (Invitrogen, #PA5-30055,

rabbit, 1:1000), total histone H2AZ (Abcam, #ab150402, rabbit, 1:1000), total histone H2B1L (St John's Laboratory, #STJ195934, rabbit, 1:1000), total histone H3 (Sigma, #H0164, rabbit, 1:1000), total histone H4 (Merck, #07-108, rabbit, 1:1000), alpha-tubulin (Sigma-Aldrich, #T6199, mouse, 1:1000). After 12h, the membranes were washed 3 times with TBST for 5 min and incubated at room temperature with a secondary antibody: IRDye anti-mouse 1:10 000 (LI-COR, Lincoln, US, P/N 926-322210 and P/N 926-68070) and IRDye anti-rabbit (LI-COR, Lincoln, US, P/N 926-32211 and P/N 926-68071) 1:10 000 for 1h. Following this step, membranes were washed 3 times with TBST for 5 min and 2 times with TBS for 10 min. Detection was carried out using an Odyssey device (LI-COR, Lincoln, US) and quantification was performed using Image Studio Lite (Version 5.2.5). All histone signals were normalized by using corresponding alpha-tubulin signals.

RT-qPCR with nematode samples.

250 synchronized AD2 stage N2 animals were harvested in 1x M9 followed by resuspension in 1 mL Tri Reagent (Sigma Aldrich, Darmstadt, Germany). Samples were homogenized using Precellys 24 device (Precellys, Bertin Technologies, France) with 2 cycles of 20 seconds/6.000 rpm, separated by a 30-sec interval. Subsequently, 5 min incubation at room temperature with 100 µL 1-Bromo-3-chloropropane (BCP) (Merck, Darmstadt, Germany, #B9673) was performed. Samples were vortexed for 15 sec and incubated for 2 min at room temperature. Then, centrifuged at 12.000 rpm for 15 min at 4ºC. The upper clear phase was collected and mixed with an equal amount of 70% EtOH in RNAse-free water (HyPure, Cytiva, Utah, US). RNA isolation was performed by using an innuPREP RNA mini kit (Analytik Jena, Jena, Germany) and following the manufacturer's instructions. The samples were further treated with DNase and RNase (Thermo Fisher Scientific, Bremen, Germany) by following the manufacturer's instructions for a reaction with 1 µg total RNA. Reverse transcription was done with 0.5 µg total RNA using RT SuperScript III kit (Invitrogen, California, US) and following the manufacturer's instructions. RT-qPCR reactions were performed in triplicates in 96-well plates, using SSoAdvanced SYBR Green master mix (Bio-Rad, California, US) and following the manufacturer's instructions in a Bio-Rad CFX96 touch real-time machine (Bio-Rad, California, US). The relative gene expression was calculated by using the $2^{-\Delta\Delta Ct}$ method (Livak & Schmittgen, 2001). The list of primers can be found in Table S24.

Analysis of DREAM binding sites at candidate genomic regions.

The previously published ChiP-Seq dataset was obtained from[6], and overlapping genome binding sites of the three DREAM subunits mediating the health effects of circadian dysfunction (LIN-9, LIN-53, and LIN-54) were searched against promoter regions of candidate genes by using the *C. elegans* genome assembly version WS220/ce10 (UCSC Genome Browser Gateway database).

Cell culture, siRNA exposure and Harmine treatment.

RPE-1 hTERT cells (#RPE CRL-4000, ATCC) were cultured in DMEM media with F12 (#31331093, Thermo Fisher Scientific). Culture media were supplemented with 10% fetal bovine serum (FBS; # A5209402 Thermo Fisher Scientific) and penicillin/streptomycin (#15140122, Thermo Fisher Scientific). Cell lines were tested at least twice a year for *Mycoplasma* contamination using the LookOut Detection Kit (Sigma), and all tests were negative.

Cells were treated with DMSO (0.1%; Carl Roth, Karlsruhe, Germany) or Harmine (10 μM; Sigma-Aldrich, SMB00461) for 20 h. For knockdown experiments, cells were reverse transfected with 10 nM Silencer Select siRNAs (Thermo Fisher Scientific) using RNAiMAX (#13778150, Fisher Scientific) and Opti-MEM (#31985062, Thermo Fisher Scientific) following the manufacturer protocol. The following siRNAs were used (Thermo Fisher Scientific): siControl (#4390844) and siPER1 (#s10301).

Reverse transcription semi-quantitative real-time PCR (RT-qPCR) in RPE cells

Total cellular RNA was extracted using the innuPREP RNA Mini Kit (Analytik Jena, Jena, Germany) following the manufacturer protocol. One-step reverse transcription and real-time PCR was performed with a Quantstudio 5 using Power SYBR Green RNA-to-CT 1-Step Kit (Thermo Fisher Scientific) following the manufacturer protocol. The list of primers used can be found in Table S25.

RNA-sequencing in RPE cells.

Total RNA was extracted from 5 replicas using the innuPREP RNA Mini Kit (Analytik Jena, Jena, Germany) following the manufacturer protocol. Sequencing of RNA samples was

performed using Illumina's next-generation sequencing methodology[7]. In detail, total RNA was quantified, and quality checked using Tapestation 4200 instrument in combination with RNA ScreenTape (both Agilent Technologies). Libraries were prepared using a Biomek i7 by introducing 300 ng of total RNA using NEBNext Ultra II Directional RNA Library Preparation Kit in combination with NEBNext Poly(A) mRNA Magnetic Isolation Module and NEBNext Multiplex Oligos for Illumina (Unique Dual Index UMI Adaptors RNA) following the manufacturer's instructions (New England Biolabs). Quantification and quality check of libraries was done using a Tapestation 4200 instrument and a D1000 ScreenTape (Agilent Technologies). Libraries were pooled and sequenced on a NovaSeq6000 SP 100 cycle run. System ran in a 101 cycle/single-end/standard loading workflow mode. Sequence information was converted to FASTQ format using bcl2fastq v2.20.0.422.

Raw read quality trimming (5nt sliding window with cutoff 20) was performed using Trimmomatic v0.39[8] and TruSeq universal adapter were clipped (minimum overlap 5nt) with Cutadapt v2.10 (minimum length 18)[9]. Potential sequencing errors were detected and corrected utilizing Rcorrector v1.0.4[10] prior to artificial rRNA depletion using SortMeRNA v2.1b[11]. Reads were aligned to the human genome with segemehl v0.3.4[12, 13] (split-read mode, accuracy 95%, reference GRCh38) and filtered for unique alignments with SAMtools v1.14[14].

Alignments have been deduplicated for over amplified PCR fragments based on unique molecular identifiers utilizing UMI-tools v1.1.1[15] and subsequently quantified with featureCounts v2.0.1 (10nt minimum exon based meta-feature overlap, reference annotation Ensembl v106)[16]. Differences (log2FC) between conditions mentioned in the figures were calculated with DESeq2 v1.34.0[17].

Statistical analysis

The raw data of all experiments were plotted in Excel sheets, GraphPad Prism, or Rstudio files. The tests used in each experiment are mentioned in respective figure legends. The differences were considered significant with *$p < 0.05$, **$p < 0.01$, ***$p < 0.001$, n.s. = not significant, unless otherwise stated.

Data availability

The mass spectrometry proteomics data have been deposited to the ProteomeXchange Consortium via the PRIDE (Perez-Riverol et al., 2019) and MassIVE repositories with the respective dataset identifiers PXD024273 and MSV000091972. The RNA-seq data have been deposited to the NCBI Gene Expression Omnibus (GEO) with data set identifier GSE250018 and reviewer token ijadosganjktvev.

Bibliography:

1. Olmedo, M. *et al.* Prolonged quiescence delays somatic stem cell-like divisions in Caenorhabditis elegans and is controlled by insulin signaling. *Aging Cell* **19**, e13085 (2020).
2. Espada, L. *et al.* Loss of metabolic plasticity underlies metformin toxicity in aged Caenorhabditis elegans. *Nat Metab* **2**, 1316-1331 (2020).
3. Olmedo, M., Geibel, M., Artal-Sanz, M. & Merrow, M. A High-Throughput Method for the Analysis of Larval Developmental Phenotypes in Caenorhabditis elegans. *Genetics* **201**, 443-448 (2015).
4. McColl, G. *et al.* Utility of an improved model of amyloid-beta (Abeta(1)(-)(4)(2)) toxicity in Caenorhabditis elegans for drug screening for Alzheimer's disease. *Mol Neurodegener* **7**, 57 (2012).
5. Morley, J.F., Brignull, H.R., Weyers, J.J. & Morimoto, R.I. The threshold for polyglutamine-expansion protein aggregation and cellular toxicity is dynamic and influenced by aging in Caenorhabditis elegans. *Proc Natl Acad Sci U S A* **99**, 10417-10422 (2002).
6. Latorre, I. *et al.* The DREAM complex promotes gene body H2A.Z for target repression. *Genes Dev* **29**, 495-500 (2015).
7. Bentley, D.R. *et al.* Accurate whole human genome sequencing using reversible terminator chemistry. *Nature* **456**, 53-59 (2008).
8. Bolger, A.M., Lohse, M. & Usadel, B. Trimmomatic: a flexible trimmer for Illumina sequence data. *Bioinformatics* **30**, 2114-2120 (2014).
9. Martin, M. Cutadapt removes adapter sequences from high-throughput sequencing reads. *EMBnet.journal* **17**, 10 (2011).
10. Song, L. & Florea, L. Rcorrector: efficient and accurate error correction for Illumina RNA-seq reads. *Gigascience* **4**, 48 (2015).
11. Kopylova, E., Noe, L. & Touzet, H. SortMeRNA: fast and accurate filtering of ribosomal RNAs in metatranscriptomic data. *Bioinformatics* **28**, 3211-3217 (2012).
12. Hoffmann, S. *et al.* A multi-split mapping algorithm for circular RNA, splicing, trans-splicing and fusion detection. *Genome Biol* **15**, R34 (2014).
13. Hoffmann, S. *et al.* Fast mapping of short sequences with mismatches, insertions and deletions using index structures. *PLoS Comput Biol* **5**, e1000502 (2009).
14. Li, H. *et al.* The Sequence Alignment/Map format and SAMtools. *Bioinformatics* **25**, 2078-2079 (2009).
15. Smith, T., Heger, A. & Sudbery, I. UMI-tools: modeling sequencing errors in Unique Molecular Identifiers to improve quantification accuracy. *Genome Res* **27**, 491-499 (2017).

16. Liao, Y., Smyth, G.K. & Shi, W. featureCounts: an efficient general purpose program for assigning sequence reads to genomic features. *Bioinformatics* **30**, 923-930 (2014).
17. Love, M.I., Huber, W. & Anders, S. Moderated estimation of fold change and dispersion for RNA-seq data with DESeq2. *Genome Biol* **15**, 550 (2014).